Microwave photonic Fano shaped spectral filters using transversal filters with microcombs

David J. Moss

***Abstract*— Microwave photonic (MWP) Fano filters, featuring asymmetric filter shapes that enable steep spectral transitions, are attractive for high-bandwidth microwave signal processing such as frequency discrimination. However, achieving both steep spectral transitions and a high degree of reconfigurability remains challenging for conventional methods relying on direct mapping of Fano resonances generated by optical filters. Here, we propose and experimentally demonstrate a new way for realizing MWP Fano filters based on a microcomb-driven transversal filter system. Leveraging the large number of comb lines provided by microcombs as discrete taps, the transversal filter system can synthesize filter response that closely resembles Fano resonances, yielding high roll-off rates and slope rates up to ~33.8 dB / GHz and ~25.7 dB / GHz in our experiments, respectively. In addition, by simply programming the tap coefficients without changing any hardware, highly reconfigurable filter response can be realized. We experimentally demonstrate independent tuning of all three Fano characteristic parameters, including the asymmetry factor, resonance linewidth, and center frequency. These results verify the effectiveness of our approach for implementing highly reconfigurable MWP Fano filters with steep spectral transitions, offering strong versatility for meeting diverse requirements in practical applications.**

***Index Terms*— Microwave photonics, optical microcombs, Fano resonance.**

I. Introduction

Microwave photonic (MWP) filters, which perform filtering functions in the microwave (MW) frequency band using photonic technologies, offer attractive advantages of broad operation bandwidths that overcomes the intrinsic bandwidth bottleneck of electronic devices, low loss that improves signal-to-noise ratios, and strong immunity to electromagnetic interference [1-4]. Nowadays, MWP filters have found wide applications for high-bandwidth MW signal processing in modern communication, radar, and sensing systems [5-8]. As a fundamental class of MWP filters, MWP Fano filters, featuring asymmetric filter shapes that enable steep spectral transitions, are particularly attractive for high-sensitivity frequency discrimination and instantaneous frequency measurement [9-11].

Conventional MWP Fano filters are typically realized by using a single optical carrier to map the response of Fano resonances generated by optical resonators into the MW domain [9-11]. In these filters, Fano resonances are generated by engineering the interference between a discrete localized state and a continuum state [12-14], and high quality (Q) factors of the optical resonators are needed to enable steep spectral transitions, thereby enhancing the sensitivity for frequency discrimination. However, the high Q factors also lead to increased sensitivity to resonance drift and fabrication tolerances, thus imposing stringent requirements on resonance alignment and thermal stabilization for long-term operation [15]. In addition, these filters usually lack reconfigurability, although minor adjustments can be made by introducing PN junctions [16, 17] or thermo-optic heaters [18, 19]. In particular, the characteristic parameters of Fano filters, including the asymmetry factor, resonance linewidth, and center frequency, are determined by multiple structural parameters of the optical resonators, making it challenging to tune one parameter independently without affecting the others. The above limitations collectively make it challenging to realize MWP Fano filters that simultaneously offer steep spectral transitions and a high degree of reconfigurability.

In this work, we propose and experimentally demonstrate MWP Fano filters based on a microcomb-driven transversal filter system, enabling both steep spectral transitions and a

David J. Moss is with the Optical Sciences Center, Swinburne University of Technology, Hawthorn, VIC 3122, Australia (dmoss@swin.edu.au).

high degree of reconfigurability. By using the large number of comb lines provided by optical microcombs as discrete taps, the transversal filter system can synthesize filter response that closely resembles Fano resonances through coherent combination of delayed and weighted taps. Experimental results show that high roll-off rates and slope rates up to ~33.8 dB / GHz and ~25.7 dB / GHz are achieved, respectively. Moreover, we experimentally demonstrate highly reconfigurable filter response by simply programming the tap coefficients without changing any hardware, achieving independent tuning of all three Fano characteristic parameters including the asymmetry factor, resonance linewidth, and center frequency. These results highlight the strong potential of our approach for implementing highly reconfigurable MWP Fano filters with steep spectral transitions, which are capable of addressing diverse requirements in practical applications.

II. Operation Principle

In this work, we investigate Fano filters exhibiting asymmetric spectral lineshapes, which were first elucidated by Fano through the well-known Fano formula as follows [20]

$$F(\varepsilon) = \frac{(q+\varepsilon)^2}{1+\varepsilon^2}, \tag{1}$$

where q is the asymmetry factor and ε is the scale of reduced energy. In **Eq. (1)**, the minimum transmission reaches 0 when $\varepsilon = -q$. In spectral filter applications, ε can be further defined as

$$\varepsilon = \frac{\omega - \omega_c}{\Gamma}, \tag{2}$$

where ω is the angular frequency, ω_c is the center angular frequency, and Γ is the resonance linewidth. By substituting $\omega = 2\pi f$, $\omega_c = 2\pi f_c$ and $\Gamma_f = \Gamma / (2\pi)$ into **Eq. (2)**, and then substituting **Eq. (2)** into **Eq (1)**, the transfer function for MW Fano filters investigated in this work can be expressed as

$$T(f) = \frac{\left(q + \frac{f - f_c}{\Gamma_f}\right)^2}{1 + \left(\frac{f - f_c}{\Gamma_f}\right)^2}, \tag{3}$$

where f, f_c, and Γ_f are the corresponding MW frequency, center frequency, and resonance linewidth, respectively.

In **Fig. 1**, we plot the spectral amplitude response of Fano filters based on **Eq. (3)**. **Fig. 1(a)** illustrates the roles of three characteristic parameters, namely q, Γ_f, and f_c, in determining the spectral lineshape of the Fano filter. Here, points A and B mark the maximum and minimum transmission at frequencies of f_A and f_B, respectively. Point C corresponds to the center frequency of f_c. As can be seen, the product of $q\Gamma_f$ jointly determines the frequency offset between points B and C, which can be expressed as

$$f_B - f_c = q\Gamma_f. \tag{4}$$

To better illustrate the relationship in **Eq. (4)**, **Figs. 1(b)**, **(c)**, and **(d)** compare the amplitude response of Fano filters with various q, Γ_f, and f_c, respectively. In each figure, all parameters other than the one being varied are kept constant. **Fig. 1(b)** shows the results for q = -1 and q = -4 at fixed $\Gamma_f = \Gamma_1$ and $f_c = f_1$. At q = -1, the response spectrum exhibits an odd-symmetric profile, in which the transmission at the center frequency f_c equals 0.5 (*i.e.*, -3 dB). According to **Eq. (4)**, it can also be obtained that $f_B - f_1 = \Gamma_1$. At q = -4, the response spectrum becomes asymmetric. Point B shifts to point B' at a higher frequency of $f_{B'}$, satisfying $f_{B'} - f_1 = 4\Gamma_1$ according to **Eq. (4)**. In addition, the transmission at f_c increases and no longer equals 0.5, which is also governed by the relationship in **Eq. (4)**. **Fig. 1(c)** shows the response spectra for $\Gamma_f = \Gamma_1$ and $\Gamma_f = 2\Gamma_1$ at fixed q = -1 and $f_c = f_1$. As Γ_f increases from Γ_1 to $2\Gamma_1$, the response spectrum remains odd-symmetric, and point B shifts to point B' at a higher frequency of $f_{B'}$. The former indicates a preserved filter symmetry, and the latter signifies an increased filtering bandwidth. **Fig. 1(d)** shows the response spectra for $f_c = f_1$ and $f_c = f_2$ at fixed q = -1 and $\Gamma_f = \Gamma_1$. The filter shape and bandwidth are identical in both cases, differing only in the center frequency. This reflects the fact that variation in f_c does not alter the filter shape and bandwidth, forming the basis for implementing Fano filters with tunable center frequencies.

In practical applications, another two parameters – the slope rate (SR) and the roll-off rate (ROR), are widely used to quantitatively compare the performance of Fano filters [9, 12, 21]. The SR is defined as [22]

$$\mathrm{SR} = \frac{ER}{|f_P - f_N|}, \tag{5}$$

where ER is the extinction ratio, *i.e.*, the attenuation from transmission peak to notch, typically expressed in units of dB. The terms f_P and f_N are the frequencies corresponding to the transmission peak and notch, respectively. The ROR is defined as [4]

$$\mathrm{ROR} = \frac{AT}{|f_T - f_R|}, \tag{6}$$

where AT is the attenuation from the -3 dB transmission point in the passband to a point corresponding to the reference level in the stopband. The terms f_T and f_R are the frequencies corresponding to these two points.

Figs. 1(e) and **1(f)** illustrate the definitions of SR and ROR in **Eqs. (5)** and **(6)**, respectively. For both SR and ROR, higher values indicate steeper transitions and sharper roll-off in the filter response, which is desirable for practical Fano filter applications [9, 11, 23]. The SR is more commonly used for optical resonators with Fano resonances [12-14], whereas the ROR is typically used in the context of MW filters.

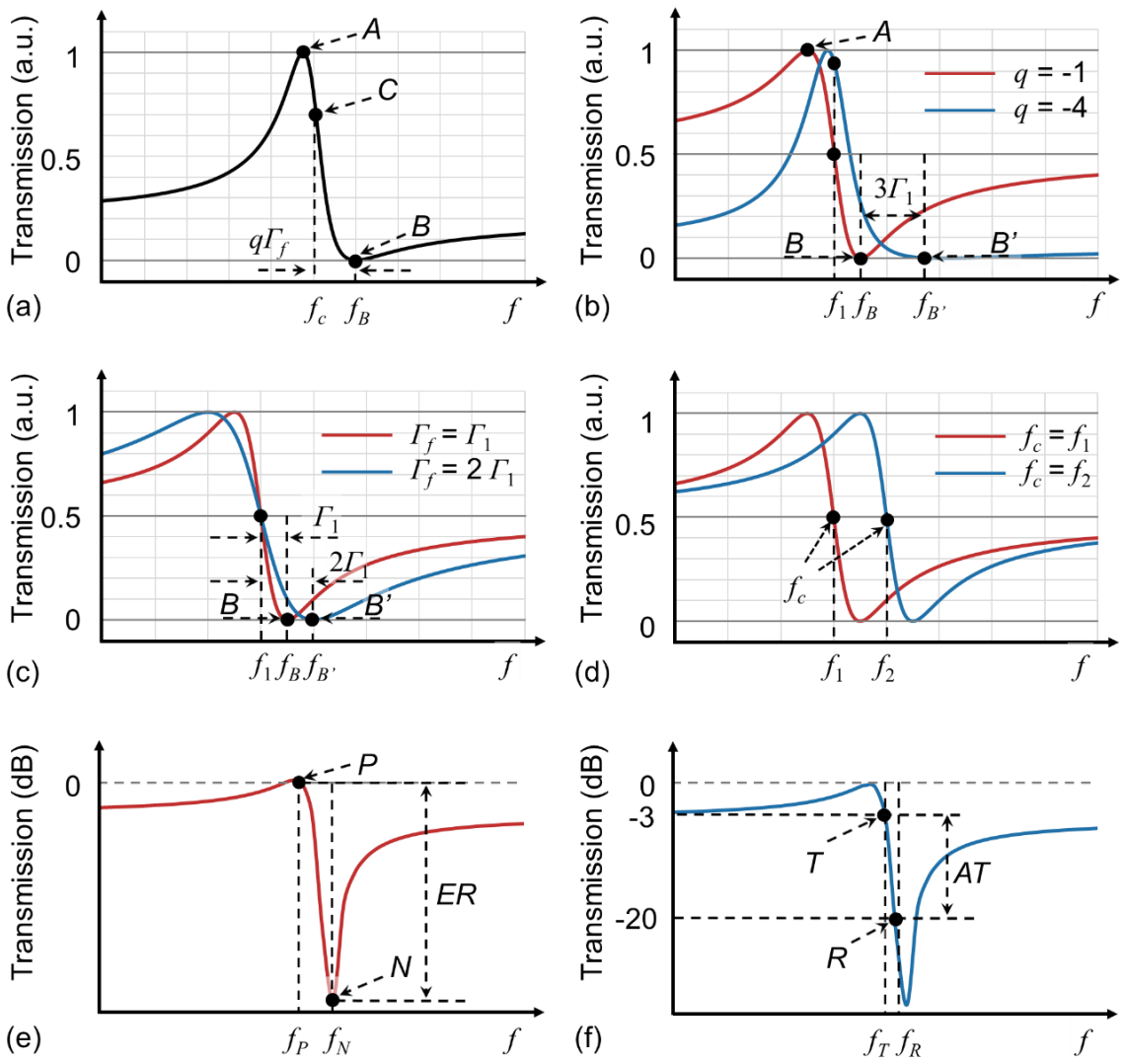


Fig. 1. Spectral response of Fano filters. (a) Amplitude response of a typical Fano filter. Points *A* and *B* mark the maximum and minimum transmission at frequencies of f_A and f_B, respectively. Point *C* corresponds to the center frequency of f_c, q is the asymmetry factor, and Γ_f is the resonance linewidth. (b) Amplitude response for q = -1 and q = -4 at fixed $f_c = f_1$ and $\Gamma_f = \Gamma_1$. (c) Amplitude response for $\Gamma_f = \Gamma_1$ and $\Gamma_f = 2\Gamma_1$ at fixed q = -1 and $f_c = f_1$. (d) Amplitude response for $f_c = f_1$ and $f_c = f_2$ at fixed q = -1 and $\Gamma_f = \Gamma_1$. (e) Illustration for the definition of slope rate (SR) for a Fano filter, where *P* and *N* mark the maximum and minimum transmission points at frequencies of f_P and f_N, respectively. (f) Illustration for the definition of roll-off rate (ROR) for a Fano filter, where *T* and *R* mark the -3 dB transmission point in the passband and a reference point in the stopband at -20 dB transmission, respectively.

To realize the Fano filters shown in **Fig. 1**, we employ a transversal filter system widely used for MW signal processing [24-30]. **Fig. 2(a)** illustrates the operation principle of a MW transversal filter system. As the input MW signal propagates through the system, a cascade of delay elements introduces time delays between adjacent signal replicas, with each delay element providing a time delay of Δt. The delayed signal replica in each channel is weighted according to the designed tap coefficient (*i.e.*, a_0, a_1, …, a_{M-1}), after which the delayed and weighted signal replicas from different channels are summed to produce the final output.

Fig. 2(b) illustrates a transversal filter system implemented based on the MWP technology. Optical microcombs generated by a compact integrated MRR is employed as a multiwavelength source for the transversal filter system. Replicas of the input MW signal are generated by modulating it onto optical carriers at different wavelength channels. The delay between adjacent wavelength channels is provided by the dispersion of a spool of single-mode fiber (SMF), and the tap coefficient in each channel is assigned using a programmable optical spectral shaper (OSS). Finally, the delayed and weighted signal replicas are summed upon photodetection to generate a MW signal as the system output.

The output MW signal $s(t)$ from the MWP transversal filter system in **Fig. 2(b)** can be expressed as

$$s(t) = f(t) * h(t) = \sum_{n=0}^{M-1} a_n f(t - n\Delta t), \tag{7}$$

where M is the total number of tap coefficient, a_n (n = 0, 1, 2, …, M - 1) is the tap coefficient of the n_{th} tap, Δt is the delay time between adjacent taps and $f(t)$ denoting the input MW signal. The temporal impulse response $h(t)$ in **Eq. (7)** can be given by

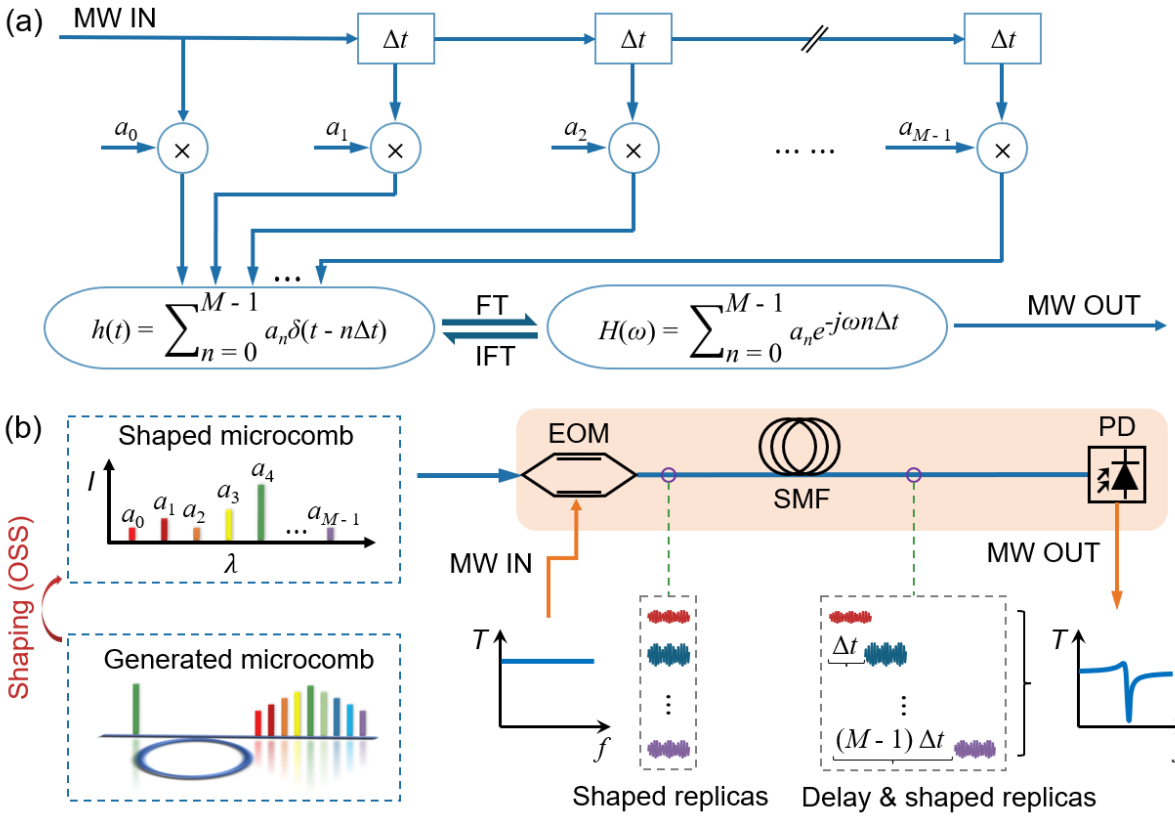


Fig. 2. Transversal filter system. (a) Schematic illustration for the operation principle of a microwave (MW) transversal filter system, where Δt is the time delay between adjacent channels, and a_0, a_1, …, a_{M-1} are the tap coefficients in each channel. FT: Fourier transform. IFT: inverse Fourier transform. (b) Schematic diagram and processing flow of a microwave photonic (MWP) transversal filter system with an optical microcomb source. OSS: Optical spectral shaper. EOM: Electro-optic modulator. PD: photodetector.

$$h(t) = \sum_{n=0}^{M-1} a_n \delta(t - n\Delta t), \tag{8}$$

where $\delta(t)$ is the unit impulse function. By applying the Fourier transform to **Eq. (8)**, the spectral transfer function of the MWP transversal filter system can be written as

$$H(\omega) = \sum_{n=0}^{M-1} a_n e^{-j\omega n\Delta t}, \tag{9}$$

Eq. (9) represents a typical transfer function for the transversal filter systems [31], which exhibits finite impulse response (FIR), and diverse filtering functions can be realized by designing the corresponding tap coefficients a_n (n = 0, 1, 2, …, M - 1). This provides the basis for implementing Fano filters shown in **Fig. 1**, enabling reconfigurable Fano filters with different asymmetry factor q, resonance linewidth Γ_f, or center frequencies f_c to be realized simply through programing the tap coefficients a_n (n = 0, 1, 2, …, M - 1).

It is also worth noting that due to the FIR nature of transversal filter systems, deviations arise between the ideal filter response and that realized based on the transfer function in **Eq. (9)** for target filters with infinite impulse response (IIR), including Fano filters investigated in this work. These deviations can also degrade the SR and ROR of Fano filters realized based on the MWP transversal filter system. However, these deviations decrease as the tap number M increases and becomes negligible when M is sufficiently large. Therefore, a large number of wavelength channels are required in practical MWP transversal filter systems to minimize these deviations and increase the SR and ROR performance. For brevity, the filters realized based on **Eq. (9)** are referred to as MWP Fano filters throughout this paper, although strictly speaking, they are synthesized filters exhibiting a Fano-like spectral response in the MW domain, rather than those based on directly mapping the Fano resonances generated by IIR optical filters [9-11].

In **Fig. 2(b)**, employing optical microcombs as the multiwavelength source offers significant advantages over conventional discrete laser arrays [32-34] and fiber Bragg grating arrays [35-37], which are constrained in the number of available taps because the system size, power consumption, and complexity increase dramatically with the tap number. In addition, compared with laser frequency combs generated by electro-optic modulation or mode-locked fiber lasers [38-40], optical microcombs provide large comb spacings owing to the small volume of the micro-resonators, enabling wide Nyquist bands between wavelength channels and hence broad operation bandwidths for the MWP transversal filters.

In **Eq. (9)**, the time delay Δt provided by the SMF in **Fig. 2(b)** can be given by [41]

$$\Delta t = L \cdot D \cdot \Delta\lambda\,, \tag{10}$$

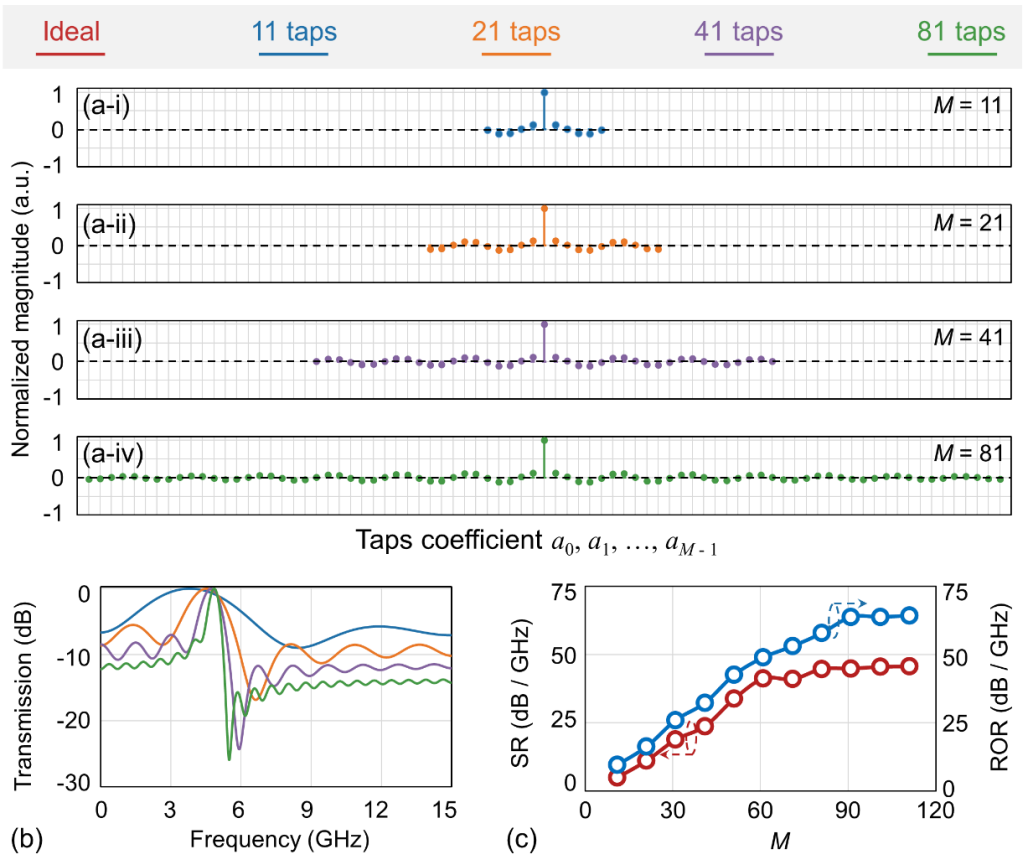


Fig. 3. Simulated spectral response of Fano filters with q = -3, Γ_f = 0.2 GHz, and f_c = 5 GHz, realized using a microcomb-based MWP transversal filter system. (a-i) – (a-iv) Designed tap coefficients for Fano filters with various tap numbers of M = 11, 21, 41, and 81, respectively. (b) Simulated amplitude response for the Fano filters in (a). (c) Slope rate (SR) and roll-off rate (ROR) versus M, which are calculated based on the results in (b).

where $\Delta\lambda$ denotes the comb spacing, D is the dispersion parameter of the SMF, and L is the length of the SMF. Since the MWP transversal filter has finite impulse response, it exhibits a periodic spectral response with a free spectral range (FSR) of $FSR_{MW} = 1 / \Delta t$. This sets an upper limit for the operation bandwidth (OBW) of the microcomb-based MWP transversal filter system, which is equal to $FSR_{MW} / 2$. In addition, according to the Nyquist sampling theorem, a bandwidth-limited continuous-time signal must be sampled at a rate exceeding twice its highest frequency component to avoid aliasing. This constraint therefore sets another upper limit on the operation bandwidth of the microcomb-based MWP transversal filter system, which is equal to half of the comb spacing (*i.e.*, $\Delta\lambda / 2$). Considering these above, the operation bandwidth (OBW) of a microcomb-based MWP transversal filter can be expressed as:

$$\mathrm{OBW} = \min\{\Delta\lambda / 2,\ FSR_{MW} / 2\}. \quad (11)$$

Fig. 3 shows simulated response of Fano filters realized using the microcomb-based MWP transversal filter system in **Fig. 2(b)**. In our simulation, the parameters in **Eq. (3)** were set to q = -3, Γ_f = 0.2 GHz, and f_c = 5 GHz. **Fig. 3(a)** shows the designed tap coefficients across different wavelength channels. Here we show the results for different tap numbers of M = 11, 21, 41 and 81. The tap coefficients (*i.e.*, a_0, a_1, a_2, …, a_{M-1}), including both positive and negative values, were calculated by applying inverse Fourier transform (IFT) to the target transfer function in **Eq. (3)**. As can be seen, the tap coefficients near the center exhibit larger absolute values and dominate the synthesis of the filter response, whereas those on both sides have smaller absolute values and contribute less significantly. This feature is determined by the temporal impulse response of ideal Fano filters.

Fig. 3(b) shows simulated amplitude response of Fano filters corresponding to the tap distributions in **Fig. 3(a)**. For M = 11, the main asymmetric Fano profile is reproduced. However, the notch remains relatively shallow, and the spectrum outside the resonance exhibits noticeable ripples, leading to limited SR and ROR. As M increases, the response exhibits a more distinct peak to notch feature, together with suppressed ripples as well as improved SR and ROR. For M = 81, a well-defined Fano lineshape with only minor ripples is observed, achieving a high ER of ~25.9 dB.

To quantitatively analyze the influence of tap number on the Fano filters, **Fig. 3(c)** plots the SR and ROR of the Fano filters versus tap number M. As expected, both SR and ROR increase monotonically with increasing M, confirming that a larger tap number yields a steeper roll-off for the Fano filters. The simulation results show that increasing M from 11 to 81 improves the SR from ~1.94 to ~41.8 dB / GHz and the ROR from ~6.56 to ~54.8 dB / GHz. As M increases beyond 81, further improvements in the SR and ROR become marginal.

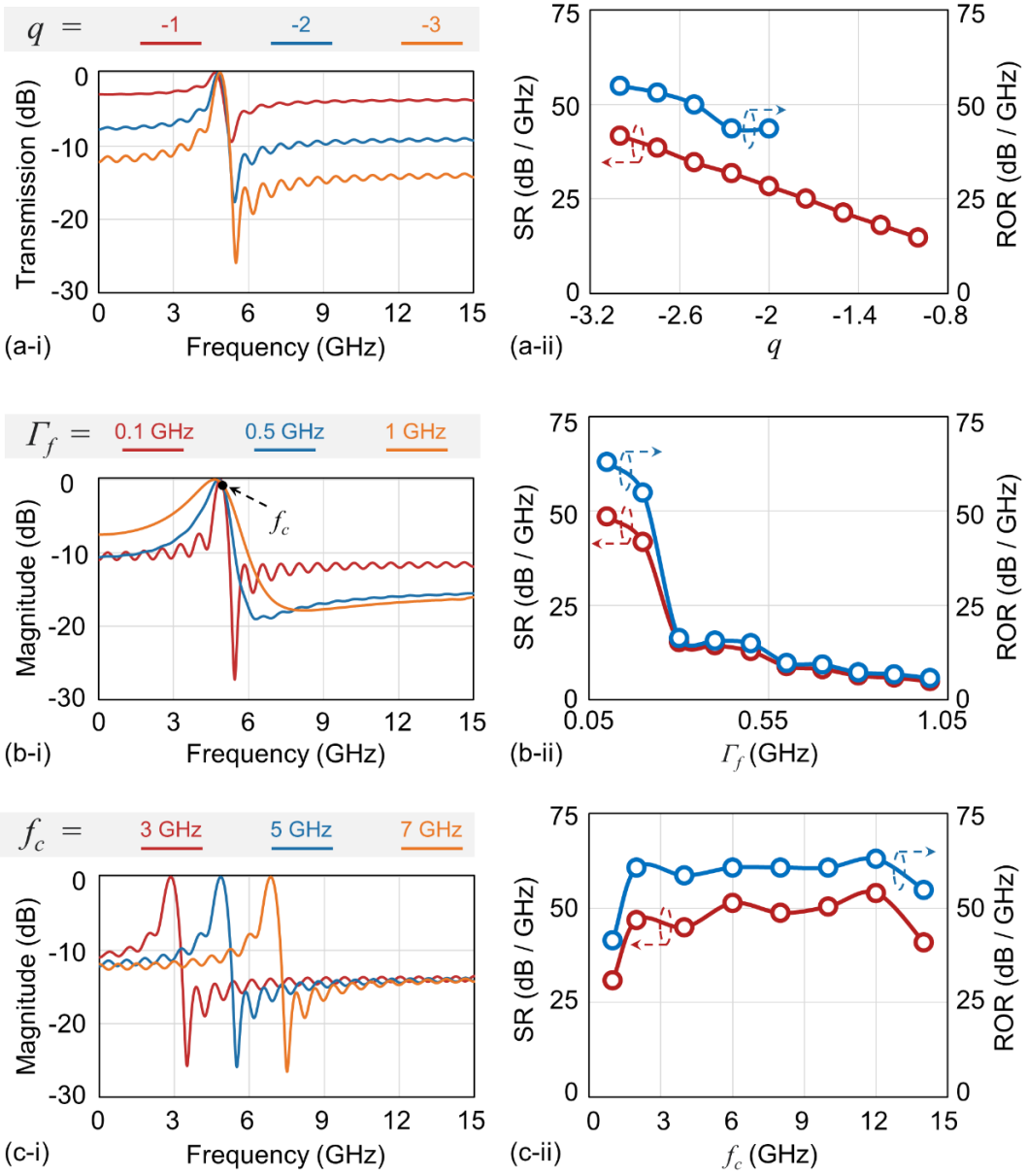


Fig. 4. Simulated response of Fano filters with various asymmetry factors q, resonance linewidth Γ_f, and center frequencies f_c, realized using a microcomb-based MWP transversal filter system. (a-i) Simulated spectral response for q = -1, -2, and -3 at fixed f_c = 5 GHz and Γ_f = 0.2 GHz. (a-ii) Calculated SR and ROR versus q. (b-i) Simulated spectral response for Γ_f = 0.1, 0.5, and 1 GHz at fixed f_c = 5 GHz and q = -3. (b-ii) Calculated SR and ROR versus Γ_f. (c-i) Simulated spectral response for f_c = 3, 5, and 7 GHz at fixed q = -3 and Γ_f = 0.2 GHz. (c-ii) Calculated SR and ROR versus f_c.

Considering this, a maximum tap number of M = 81 is chosen for our following experimental demonstrations.

Fig. 4 shows simulated response of reconfigurable Fano filters with various asymmetry factors q, resonance linewidth Γ_f and, center frequencies f_c, realized using the microcomb-based MWP transversal filter system in **Fig. 2(b)**. **Fig. 4(a-i)** shows the results for q = -1, -2 and -3 at fixed f_c = 5 GHz and Γ_f = 0.2 GHz. As q changes from -1 to -3, the filter shape becomes increasingly asymmetric, together with an increase in the *ER*. **Fig. 4(a-ii)** shows the calculated SR and ROR versus q over a range of $-1 \leq q \leq -3$. The stopband reference level was set to -20 dB for the ROR calculation according to **Eq. (6)**, and we did not plot the ROR values for $q > -2$ because the stopband response remains above this reference level. Both the SR and the ROR increase as the absolute value of q increases – consistent with the trend in **Fig. 1(b)**. **Fig. 4(b-i)** shows the results for Γ_f = 0.1, 0.5, and 1 GHz at fixed f_c = 5 GHz and q = -3. According to the relationship governed by **Eq. (4)**, the frequency offset from f_c to the minimum transmission point equals $3\Gamma_f$. Therefore, the filter exhibits the steepest roll-off at the lowest Γ_f = 0.1 GHz. The corresponding SR and ROR in **Fig. 4(b-ii)** decrease with increasing Γ_f, further confirming this trend. **Fig. 4(c-i)** shows the results for f_c = 3, 5, and 7 GHz at fixed q = -3 and Γ_f = 0.2. The filter shape and bandwidth remain unchanged, with only the center frequency position shifting – consistent with the results in **Fig. 1(d)**. This is also reflected in the nearly flat SR and ROR curves in **Fig. 4(c-ii)**. We also note that the SR and ROR curves exhibit slight

degradation on both sides due to the finite impulse response of the transversal filter system. At low f_c, the filter response approaches the resolution limit, whereas at high f_c it is constrained by the upper limit of the operating bandwidth, leading to reduced SR and ROR in both cases.

III. Experimental setup

Based on the theory in **Section II**, we performed experimental demonstrations for reconfigurable MWP Fano filters based on optical microcombs. **Fig. 5** shows a schematic of the experimental setup. A tunable continuous-wave (CW) laser was amplified by an erbium-doped fiber amplifier (EDFA) and served as the pump light. The polarization of the pump light was adjusted by a polarization controller (PC) before being coupled into a nonlinear MRR to generate optical microcombs. A temperature controller (TC) was employed to stabilize the chip temperature, thereby ensuring long-term stable microcomb generation. The initially generated microcomb exhibited non-uniform comb line powers, with higher powers in primary comb lines and lower powers in other wavelength channels. Therefore, an OSS was employed to flatten the comb lines.

The flattened optical microcomb was first amplified by another EDFA and then sent to the transversal filter module consisting of a PC, an EOM, a spool of single-mode fibre (SMF), another OSS, and a balanced photodetector (BPD). The EOM, SMF, and OSS served the same functions as those discussed in **Fig. 2(b)**. The PC was employed to optimize the modulation efficiency of the polarization-sensitive EOM. Compared with the PD in **Fig. 2(b)**, the BPD performed a similar function but was connected to the two complementary output ports of the OSS. This separated the wavelength channels into two groups and introduced a π phase shift between them, thus allowing both positive and negative tap coefficients. A vector network analyzer (VNA, Rohde & Schwarz) was employed to measure the response of the MWP transversal filter system. An optical spectrum analyzer (OSA, Anritsu) was used to measure the power of the shaped comb lines. We also employed a two-stage feedback control strategy, including synergic spectral power reshaping and impulse response reshaping as detailed in Ref. [42], to minimize the errors induced by imperfect response of experimental components and improve the accuracy of comb line shaping.

In our experimental demonstration, soliton crystal microcombs generated by an integrated doped silica MRR were employed as the microcomb source. **Fig. 6(a)** shows a schematic of the doped silica MRR. The radius of the MRR is ~592 μm. Two bus waveguides are coupled to the central micro-ring, forming a four-port device. **Fig. 6(b)** illustrates the generation of soliton crystal optical microcombs from the MRR in **Fig 6(a)**. The drop port of the MRR is employed as the output port due to its inherent filtering effect that suppresses noise in the generated optical microcombs. Soliton crystal microcombs are a distinct class of optical microcomb in which multiple co-circulating solitons spontaneously self-organize into an ordered, crystal-like pattern along the MRR [29, 30].

Fig. 6(c) shows a microscope image of the fabricated MRR. The MRR was fabricated on a doped silica platform using complementary metal-oxide-semiconductor (CMOS) compatible processes [43, 44]. Doped silica films with a refractive index of ~1.7 at 1550 nm were first deposited by plasma-enhanced chemical vapor deposition (PECVD), patterned by deep ultraviolet (UV) photolithography, and etched via reactive ion etching (RIE) to form low roughness waveguides. A silica upper cladding layer with a refractive index of ~1.44 at 1550 nm was then deposited. The doped silica platform offers low linear propagation loss of ~0.06 dB · cm^{-1}, a moderately high optical nonlinear parameter of ~233 W^{-1} · km^{-1}, and negligible nonlinear optical loss even at intensities up to 25 GW · cm^{-2}. The fabricated MRR had a high quality (Q) factor of ~1.9 million and an FSR of ~0.4 nm (*i.e.*, ~49 GHz). After packaging the MRR with fiber pigtails at the input and output ports, the coupling loss was less than 1 dB per facet.

Fig. 6(d) shows the optical spectrum of soliton crystal microcomb generated by the MRR in **Fig. 6(c)**. The comb spacing was ~0.4 nm (*i.e.*, ~49 GHz). The optical microcomb was generated from the MRR by amplifying a CW pump to ~32.1 dBm and sweeping it from shorter to longer wavelengths across a TE-polarized resonance near 1551.3 nm. As the detuning between the pump and the cold-cavity resonance decreased, the intracavity power increased and exceeded the threshold for modulation instability (MI), which initiated MI oscillations [45]. Primary comb lines were then generated, with the initial comb spacing set by the MI gain peak that is mainly governed by the cavity dispersion and the intracavity power. By further increasing the pump detuning, featured fingerprint-like spectra for soliton crystal microcombs were observed, showing agreement with those reported in Refs. [46-48]. Compared with dissipative Kerr solitons [4, 41], soliton crystal microcombs experience minimal intracavity energy variation during their formation, which enables simple and robust initiation by adiabatically sweeping the pump wavelength via manual detuning [4, 30]. **Fig. 6(e)** shows a zoom in view of the microcomb spectrum in **Fig. 6(d)** within the telecom C band (*i.e.*, 1530 nm – 1565 nm). Owing to the relatively small FSR of the MRR, a total of 90 comb lines fall within the C band, providing sufficient taps for achieving high accuracy of the transversal filter system.

For experimental setup in **Fig. 5**, the length and dispersion of the SMF were L = 4.8 km and D = 17.4 ps · nm^{-1} · km^{-1}, respectively. These, together with the comb spacing of $\Delta\lambda$ = 0.4 nm in **Fig. 6(d)**, result in a time delay of $\Delta t = L \cdot D \cdot \Delta\lambda$ = ~0.033 ns between adjacent wavelength channels and an MW FSR of $FSR_{MW} = 1 / \Delta t$ = ~30 GHz. According to **Eq. (8)**, the OBW of the practical microcomb-based MWP transversal filter system is OBW = min $\{\Delta\lambda / 2, FSR_{MW} / 2\}$ = min {~24.5 GHz, ~15 GHz} = ~15 GHz.

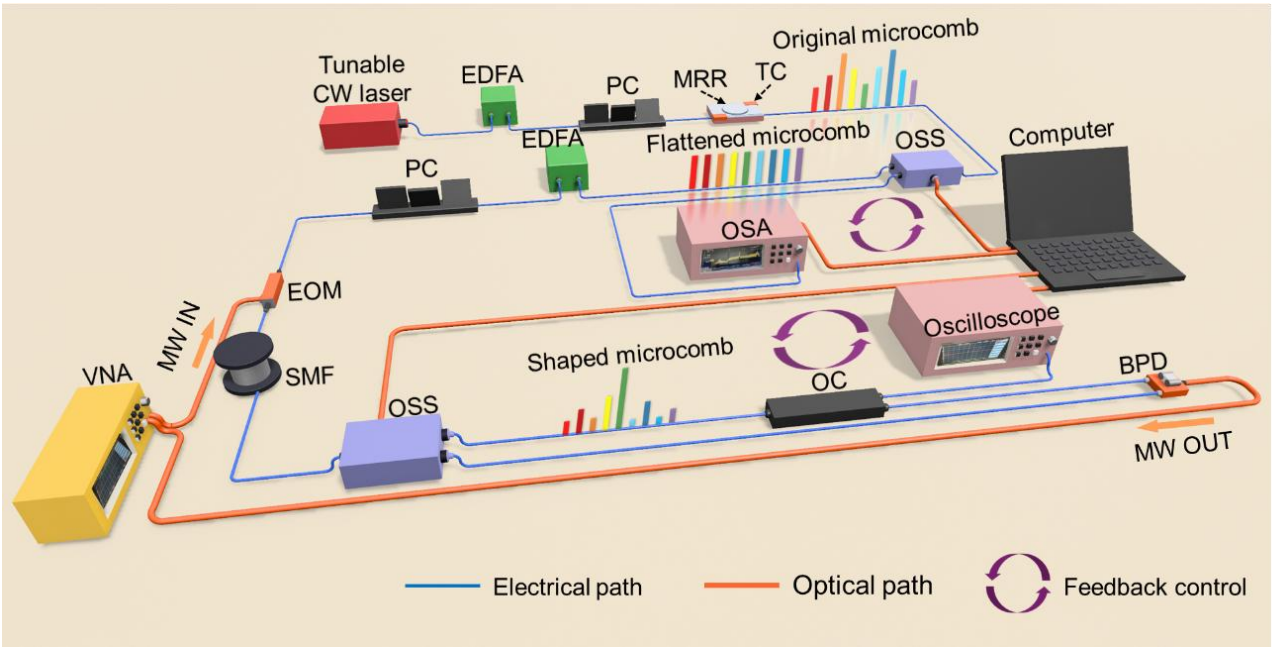


Fig. 5. Schematic of the experimental setup for demonstrating reconfigurable microcomb-based MWP Fano filters. CW laser: continuous-wave laser. EDFA: erbium-doped fiber amplifier. PC: polarization controller. MRR: micro-ring resonator. TC: temperature controller, OSS: optical spectral shaper. OSA: optical spectrum analyzer. EOM: electro-optic modulator. SMF: single-mode fiber. OC: optical coupler. BPD: balanced photodetector. VNA: vector network analyzer.

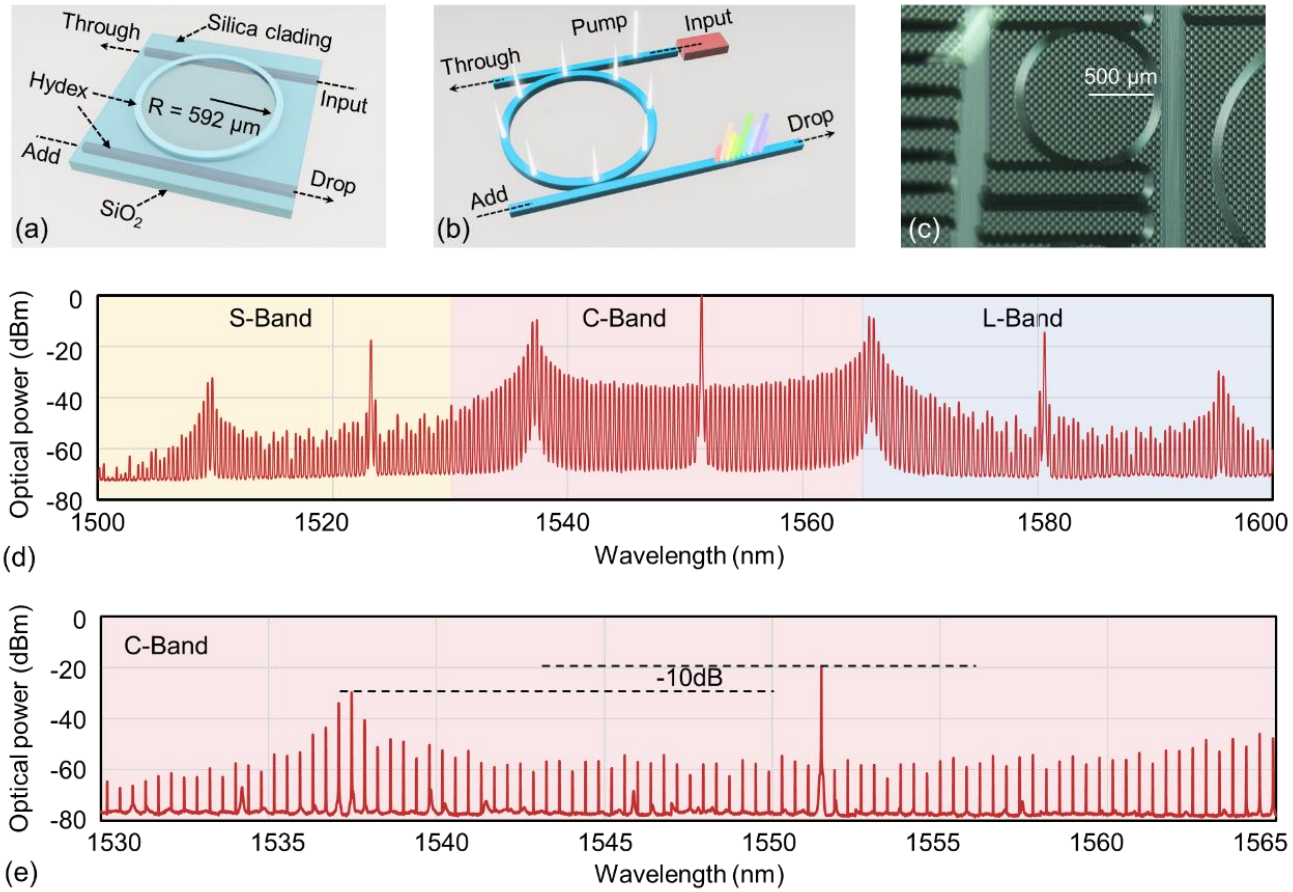


Fig. 6. Optical microcomb generation. (a) Schematic of a doped silica MRR used for optical microcomb generation. (b) Schematic illustration of optical microcomb generation from the MRR in (a). (c) Microscope image of the fabricated doped silica MRR. (d) Optical spectrum of soliton crystal microcomb generated by the MRR in (c). (e) Zoom-in view of the spectrum in (d) within telecom C band.

IV. Experimental results and discussion

By using the experimental setup discussed in **Section III**, we performed demonstrations for reconfigurable MWP Fano filters. In this section, we present and discuss the experimental results, including the filter response for various tape numbers and reconfigurable filter response with varying characteristic parameters.

Fig. 7 shows the results for MWP Fano filters with various tap numbers of M = 11, 21, 41, and 81. For comparison, the characteristic parameters of the Fano filters were fixed at f_c = 5 GHz, q = -3, and Γ_f = 0.2 GHz. **Figs. 7(a-i) – (a-iv)** show the designed tap coefficients (circles) and measured optical spectra of shaped comb lines (solid lines) for M = 11, 21, 41, and 81, respectively. The yellow circles and lines represent positive tap coefficients, whereas the orange circles and lines correspond to negative tap coefficients. As the tap number increases, more comb lines of the generated microcomb were utilized for the transversal filter, enabling a closer approximation to the ideal Fano filter transfer function in **Eq. (3)**.

Fig. 7(b) shows measured amplitude response of the Fano filters corresponding to the results in **Fig. 7(a)**, which was measured by the VNA in **Fig. 5**. At M = 11, the filter response exhibits a low *ER* of ~7.19 dB, together with a gradual spectral roll-off. As M increases, the *ER* increases and the roll-off becomes steeper, in agreement with the simulation results in **Fig. 3(b)**. **Fig. 7(c)** shows the calculated SR and ROR versus M based on the results in **Fig. 7(b)**. To facilitate comparison of the experimental results, the stopband reference level was set to -13 dB when calculating the ROR based on **Eq. (6)**, and the ROR was not evaluated in cases where the minimum transmission exceeded this reference level. As M increases from 11 to 81, the *SR* increases monotonically from ~1.4 to ~25.7 dB/GHz. For M > 41, the increase in SR becomes marginal, and a similar trend was observed for the ROR reaching a maximum value of ~33.8 dB / GHz at M = 81. These are consistent with the simulation results in **Fig. 3(c)**, further confirming that the taps near the center contribute more significantly to shape the filter response. Considering this, we choose a fixed tap number of M = 41 for the demonstration of reconfigurable MWP Fano filters in **Fig. 8**.

Fig. 8 shows the results for MWP Fano filters with reconfigurable characteristic parameters. In our experiments, we demonstrated independent tuning of the asymmetry factor q, resonance linewidth Γ_f, and center frequency f_c, which was achieved by programing the tap coefficients allocated to different wavelength channels without changing any hardware. For comparison, only one characteristic parameter varied and the other two remained unchanged.

Fig. 8(a-i) shows the measured amplitude response of the Fano filters for q = -1, -2, and -3 at f_c = ~5 GHz and Γ_f = ~0.2 GHz. As q changed from -1 to -3, the response became more asymmetric, accompanied by an increase in the *ER*. These trends are consistent with those observed in **Fig. 4(a-i)**. **Fig. 8(a-ii)** shows the calculated SR and ROR versus q based on the results in **Fig. 8(a-i)**. We do not plot the ROR values for q < -1 because the stopbands remain above the -13 dB reference level. High SR and ROR values are achieved at q = -3, and the *SR* decreases from ~22.4 to ~12.3 dB / GHz as q varies from -3 to -1. The latter exhibits a trend that agrees well with the simulation results in **Fig. 4(a–ii)**.

Fig. 8(b-i) shows the measured amplitude response for Γ_f = ~0.2, ~0.8, and ~2.5 GHz at fixed f_c = ~5 GHz and q = -3. As Γ_f increased, the spectral interval between the resonance peak and notch widened, resulting in a degraded spectral roll-off between them. These trends are consistent with those observed in **Fig. 4(b-i)**. **Fig. 8(b-ii)** shows the calculated *SR* and *ROR* versus Γ_f based on the results in **Fig. 8(b-i)**. Both the *SR* and *ROR* decrease with increasing Γ_f – in agreement with the trends for the simulation results in **Fig. 4(b-ii)**.

Fig. 8(c-i) shows the measured response for f_c = ~3, ~5, and ~7 GHz at fixed q = -3 and Γ_f = ~0.2 GHz. As f_c increased, the filter shape and bandwidth remain largely unchanged, with only the center frequency shifting towards higher frequencies – consistent with the simulation results in **Fig. 4(c-i)**. **Fig. 8(c-ii)** shows the calculated *SR* and *ROR* versus Γ_f based on the results in **Fig. 8(c-i)**. Both *SR* and *ROR* exhibit minimal changes as f_c increased, agreeing with the simulation results in **Fig. 4(c-ii)**. The minor fluctuations are mainly attributed to the non-ideal response of the experimental instruments, as will be elaborated subsequently.

Compared to previous works on MWP Fano filters [9, 21], our filter demonstrated in this work, based on a transversal filter system with an optical microcomb source, exhibits a very high degree of reconfigurability. By simply programming the tap coefficients, the filter response can be reconfigured to realize different Fano characteristic parameters (*i.e.*, q, Γ_f, and f_c), without any changes to the hardware. In contrast to MWP Fano filters realized by mapping the response of IIR optical filters into the MW domain [9-11], our method not only enables independent tuning of all three characteristic parameters, but also avoids the needs for complex mode interference, precise resonance alignment, and additional temperature control to preserve the Fano filter shape. The large number of taps provided by the optical microcombs also yield much steeper spectral transitions for our Fano filter, achieving ROR and SR values of up to ~33.8 dB / GHz and ~25.7 dB / GHz, respectively – substantially higher than the reported ROR values of ~ 7 dB / GHz [49] and ~10.2 dB / GHz [50], and SR values of ~3 dB / GHz [9] and 8 dB / GHz [21] in previous studies. This advantage makes our MWP Fano filter particularly compelling for high-sensitivity frequency discrimination applications [9, 11].

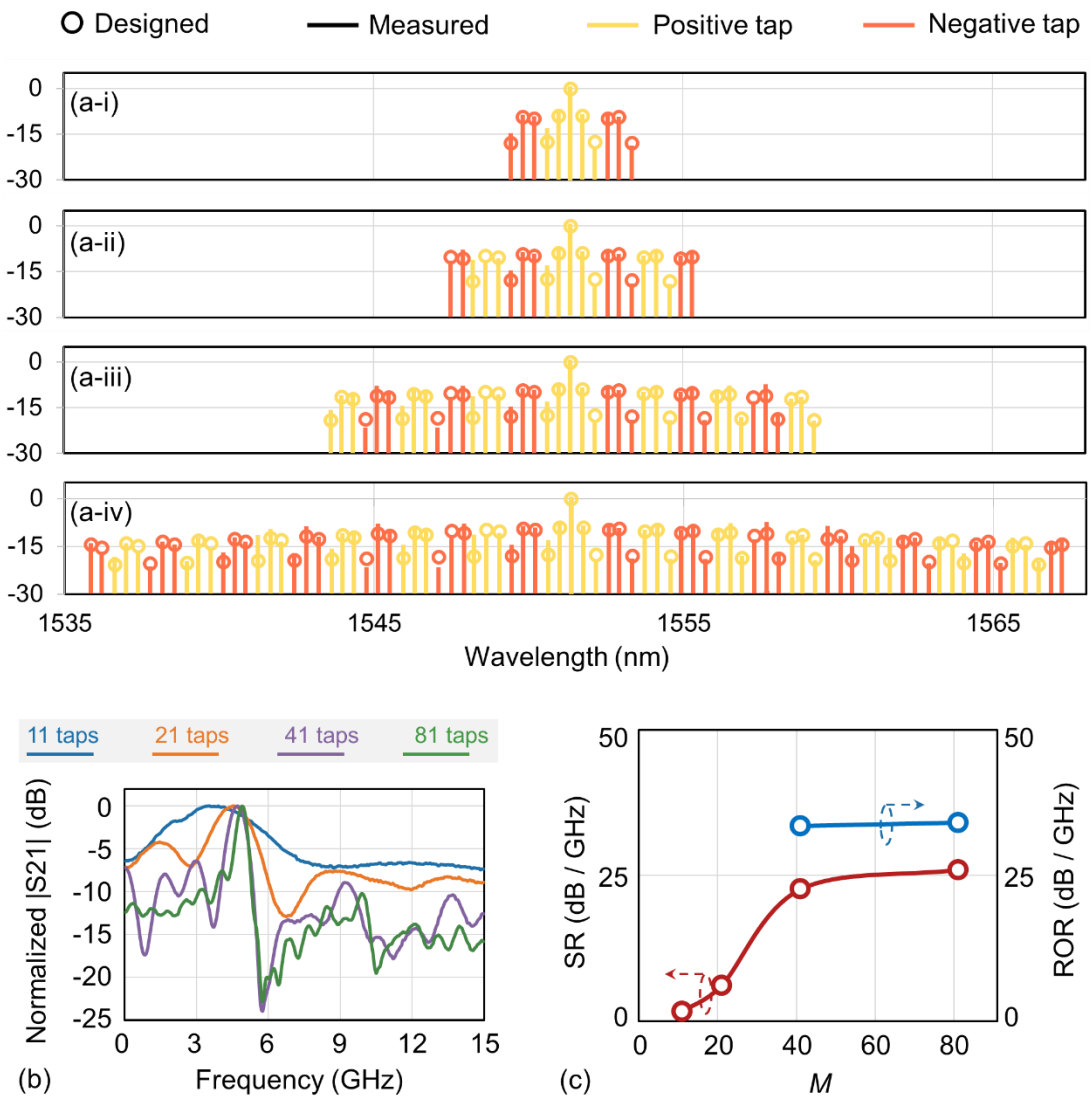


Fig. 7. Experimental results of MWP Fano filters with various tap numbers of M = 11, 21, 41, and 81. (a) Designed tap coefficients (circles) and measured optical spectra of shaped comb lines (solid lines) for (i) M = 11, (ii) M = 21, (iii) M = 41, and (iv) M = 81, where yellow circles and lines represent positive tap coefficients, and orange circles and lines correspond to negative tap coefficients. (b) Measured MW amplitude response corresponding to the results in (a). (c) SR and ROR versus M calculated based on the results in (b). In (a) – (c), the Fano characteristic parameters are q = -3, Γ_f = 0.2 GHz, and f_c = 5 GHz.

The discrepancies between the filter response obtained in our experiments and the ideal Fano filter response in **Fig. 1** arise from two sources, namely, theoretical approximation and imperfect response of a practical system. The former refers to the theoretical approximation of a filter with an infinite impulse response (which corresponds to infinite tap number) using a practical transversal filter system with a finite tap number. The latter refers to errors induced by imperfect performance of different components in the practical transversal filter system, such as the noise of microcomb, chirp of the EOM, high-order dispersion of the SMF, shaping errors of the OSS, and noise of the BPD. In our case, the discrepancies induced by theoretical approximation were largely mitigated by employing a sufficiently large tap number M (up to 81, as discussed in **Fig. 3**) and ensuring that the filter operates within the OBW (~15 GHz, as defined in **Eq. (11)**). Therefore, the discrepancies were mainly attributed to experimental imperfections. As demonstrated in our previous work [42, 51, 52], static and slowly varying errors arising from the imperfect response of the EDFA, OSSs, EOM, SMF, and BPD can be mitigated by introducing feedback control into the transversal filter system (as described in **Section III**). However, such feedback control cannot compensate for rapidly varying error sources, such as noise from the microcomb and BPD. As a result, there are still remaining discrepancies, which could be further reduced by employing advanced mode-locking techniques to suppress microcomb noise [53] and introducing gradient-descent-based control for improved calibration [54].

Monolithic integration of the microcomb-based MWP transversal filter systems represents a promising direction that has witnessed substantial progress in recent years [55, 56]. Although just replacing discrete laser arrays with compact integrated microcomb sources already offers substantial advantages in terms of SWaP, cost, and system complexity, further benefits can be realized by increasing the level of

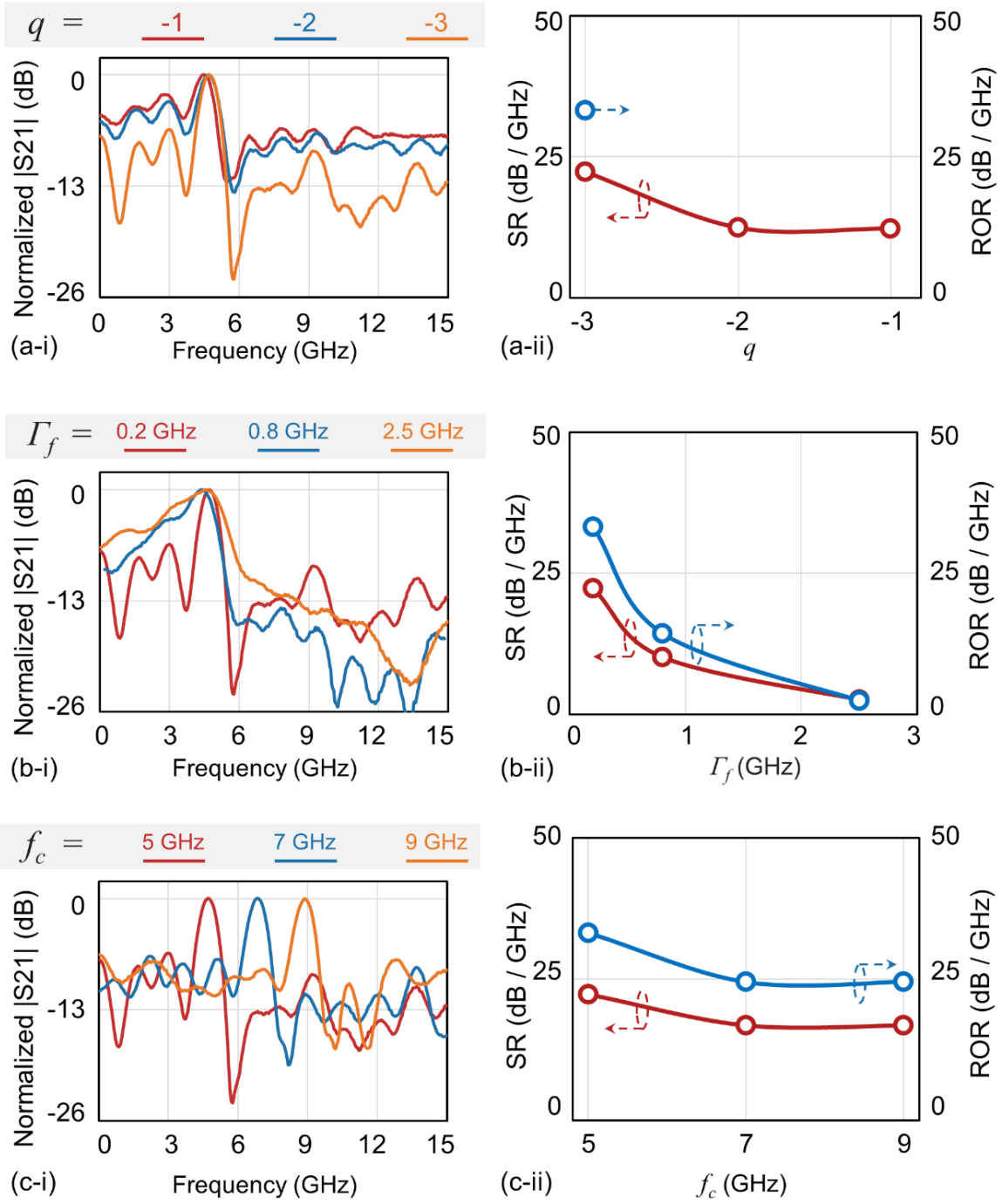


Fig. 8. Experimental results of reconfigurable MWP Fano filters. (a-i) Measured MW amplitude response for q = -1, -2 and -3 at fixed f_c = 5 GHz and Γ_f = 0.2 GHz. (a-ii) Calculated SR and ROR based on the results in (a-i). (b-i) Measured MW amplitude response for Γ_f = 0.2, 0.8 and 2.5 GHz at fixed f_c = 5 GHz and q = -3. (b-ii) Calculated SR and ROR based on the results in (b-i). (c-i) Measured MW amplitude response for f_c = 5, 7 and 9 GHz at fixed q = -3 and Γ_f = 0.2 GHz. (c-ii) Calculated SR and ROR based on the results in (c-i).

integration across the entire system. On-chip integration of the dispersive delay elements can be realized using spiral waveguide arrays [55] and chirped Bragg gratings [57]. Integrated EOM can be implemented using silicon or lithium niobate modulators [58]. Programmable spectral shaping based on MRR arrays [59] and integrated photodetectors [60] have also been demonstrated. Together, these advances pave the way towards the realization of monolithically integrated microcomb-based MWP Fano filters.

Finally, it is worth noting that, compared with on-chip microcomb-based transversal filter systems, implementing such systems based on discrete components offers distinct advantages. Fully integrating the entire system on-chip using state-of-the-art technologies would result in a substantial degradation in performance [61]. Although commercial Waveshapers are relatively bulky and power consuming compared with on-chip spectral shapers, they are highly mature products that offer outstanding stability and operate

without the need for precise alignment or stringent temperature control. In contrast, most existing on-chip spectral shapers are based on MRR arrays [59], which require additional microheaters to finely tune each resonator's wavelength to match individual comb lines. This requirement severely constrains the achievable tap number in fully integrated systems. This work has broad implications for microcombs [62-92] and their applications to microwave photonics, neuromorphic processors and communications. [93-143] The addition and use of 2D materials [144-189] will add extra functionality to microcomb chips for potential applications to quantum photonics [190 - 205] and other areas. [206-217]

V. Conclusion

In summary, we propose and experimentally demonstrate highly reconfigurable MWP Fano filters with steep spectral transitions based on a microcomb-driven transversal filter system. Benefitting from the large number of comb lines provided by optical microcombs, the transversal filter system can synthesize filter response that closely resembles Fano resonances. In addition, the filter response is highly reconfigurable by simply programming the tap coefficients without changing any hardware. In our experiments, we demonstrate steep spectral transitions for our MWP Fano filters, achieving high roll-off rates and slope rates up to ~33.8 dB / GHz and ~25.7 dB / GHz, respectively. We also demonstrate a high degree of reconfigurability for the filter response, achieving independent tuning of all three Fano characteristic parameters including the asymmetry factor, resonance linewidth, and center frequency. The MWP Fano filters in this work provide a new route towards realizing highly reconfigurable MWP Fano filters with steep spectral transitions, which are versatile for addressing varied requirements in practical applications.

References

[1] J. Capmany, and D. Novak, "Microwave photonics combines two worlds," *Nature Photonics,* vol. 1, no. 6, pp. 319-330, 2007.

[2] D. Marpaung, J. Yao, and J. Capmany, "Integrated microwave photonics," *Nature Photonics,* vol. 13, no. 2, pp. 80-90, 2019.

[3] Y. Liu, A. Choudhary, D. Marpaung, and B. J. Eggleton, "Integrated microwave photonic filters," *Advances in Optics and Photonics,* vol. 12, no. 2, pp. 485-555, 2020/06/30, 2020.

[4] Y. Li, Y. Sun, J. Wu, C. Prayoonyong, C. E. Murray, G. Ren, T. G. Nguyen, X. Xu, B. Corcoran, S. T. Chu, B. E. Little, R. Morandotti, A. Mitchell, and D. J. Moss, "Reconfigurable Microwave Photonic Filters with Ultrasteep Roll‐Off Based on Optical Microcombs," *Laser & Photonics Reviews*, 2026.

[5] J. Yao, "Microwave Photonics," *Journal of Lightwave Technology,* vol. 27, no. 3, pp. 314-335, 2009.

[6] R. A. Minasian, E. H. Chan, and X. Yi, "Microwave photonic signal processing," *Opt Express,* vol. 21, no. 19, pp. 22918-36, Sep 23, 2013.

[7] J. Capmany, J. Mora, I. Gasulla, J. Sancho, J. Lloret, and S. Sales, "Microwave Photonic Signal Processing," *Journal of Lightwave Technology,* vol. 31, no. 4, pp. 571-586, 2013.

[8] S. Pan, and Y. Zhang, "Microwave Photonic Radars," *Journal of Lightwave Technology,* vol. 38, no. 19, pp. 5450-5484, 2020/10/01, 2020.

[9] Z. Dai, P. Li, and J. Yao, "Silicon Photonic Integrated Fano Resonator With Increased Slope Rate for Microwave Signal Processing," *Journal of Lightwave Technology,* vol. 40, no. 20, pp. 6911-6918, 2022.

[10] B. Zhu, W. Zhang, S. Pan, and J. Yao, "High-Sensitivity Instantaneous Microwave Frequency Measurement Based on a Silicon Photonic Integrated Fano Resonator," *Journal of Lightwave Technology,* vol. 37, no. 11, pp. 2527-2533, 2019/06/01, 2019.

[11] Y. Tao, F. Yang, Z. Tao, L. Chang, H. Shu, M. Jin, Y. Zhou, Z. Ge, and X. Wang, "Fully On‐Chip Microwave Photonic Instantaneous Frequency Measurement System," *Laser & Photonics Reviews,* vol. 16, no. 11, 2022.

[12] M. F. Limonov, M. V. Rybin, A. N. Poddubny, and Y. S. Kivshar, "Fano resonances in photonics," *Nature Photonics,* vol. 11, no. 9, pp. 543-554, 2017.

[13] H. Arianfard, J. Wu, S. Juodkazis, and D. J. Moss, "Advanced Multi-Functional Integrated Photonic Filters Based on Coupled Sagnac Loop Reflectors," *Journal of Lightwave Technology,* vol. 39, no. 5, pp. 1400-1408, 2021.

[14] H. Arianfard, J. Wu, S. Juodkazis, and D. J. Moss, "Three Waveguide Coupled Sagnac Loop Reflectors for Advanced Spectral Engineering," *Journal of Lightwave Technology,* vol. 39, no. 11, pp. 3478-3487, 2021/06/01, 2021.

[15] W. Bogaerts, P. De Heyn, T. Van Vaerenbergh, K. De Vos, S. Kumar Selvaraja, T. Claes, P. Dumon, P. Bienstman, D. Van Thourhout, and R. Baets, "Silicon microring resonators," *Laser & Photonics Reviews,* vol. 6, no. 1, pp. 47-73, 2011.

[16] Q. Xu, B. Schmidt, S. Pradhan, and M. Lipson, "Micrometre-scale silicon electro-optic modulator," *Nature,* vol. 435, no. 7040, pp. 325-7, May 19, 2005.

[17] X. Sun, L. Zhou, J. Xie, Z. Zou, L. Lu, H. Zhu, X. Li, and J. Chen, "Tunable silicon Fabry-Perot comb filters formed by Sagnac loop mirrors," *Optics Letters,* vol. 38, no. 4, pp. 567-569, 2013/02/15, 2013.

[18] H. Yan, Y. Xie, L. Zhang, and D. Dai, "Wideband‐Tunable on‐Chip Microwave Photonic Filter with Ultrahigh‐Q U‐Bend‐Mach–Zehnder‐Interferometer‐Coupled Microring Resonators," *Laser & Photonics Reviews,* vol. 17, no. 11, 2023.

[19] J. Wu, P. Cao, T. Pan, Y. Yang, C. Qiu, C. Tremblay, and Y. Su, "Compact on-chip 1× 2 wavelength selective switch based on silicon microring resonator with nested pairs of subrings," *Photonics Research,* vol. 3, no. 1, pp. 9-14, 2015/02/01, 2015.

[20] I. Avrutsky, R. Gibson, J. Sears, G. Khitrova, H. M. Gibbs, and J. Hendrickson, "Linear systems approach to describing and classifying Fano resonances," *Physical Review B,* vol. 87, no. 12, 2013.

[21] H. Arianfard, S. Juodkazis, D. J. Moss, and J. Wu, "Sagnac interference in integrated photonics," *Applied Physics Reviews,* vol. 10, no. 1, 2023.

[22] A. Li, and W. Bogaerts, "Using Backscattering and Backcoupling in Silicon Ring Resonators as a New Degree of Design Freedom," *Laser & Photonics Reviews,* vol. 13, no. 6, 2019.

[23] H. Li, J. Su, X. Li, Y. Yang, Y. Wang, S. Shi, Q. Qiu, and Z. Fan, "Photonic-Assisted Microwave Frequency Measurement Based on Frequency-to-Time and Frequency-to-Power Mapping," *Journal of Lightwave Technology,* vol. 44, no. 1, pp. 171-179, 2026.

[24] X. Xu, J. Wu, M. Shoeiby, T. G. Nguyen, S. T. Chu, B. E. Little, R. Morandotti, A. Mitchell, and D. J. Moss, "Reconfigurable broadband microwave photonic intensity differentiator based on an integrated optical frequency comb source," *APL Photonics,* vol. 2, no. 9, 2017.

[25] M. Tan, X. Xu, B. Corcoran, J. Wu, A. Boes, T. G. Nguyen, S. T. Chu, B. E. Little, R. Morandotti, A. Mitchell, and D. J. Moss, "RF and Microwave Fractional Differentiator Based on Photonics," *IEEE*

Transactions on Circuits and Systems II: Express Briefs, vol. 67, no. 11, pp. 2767-2771, 2020.

[26] M. Tan, A. Mitchell, D. J. Moss, X. Xu, B. Corcoran, J. Wu, A. Boes, T. G. Nguyen, S. T. Chu, B. E. Little, and R. Morandotti, "Microwave and RF Photonic Fractional Hilbert Transformer Based on a 50 GHz Kerr Micro-Comb," *Journal of Lightwave Technology,* vol. 37, no. 24, pp. 6097-6104, 2019.

[27] M. Tan, X. Xu, A. Boes, B. Corcoran, J. Wu, T. G. Nguyen, S. T. Chu, B. E. Little, A. J. Lowery, R. Morandotti, A. Mitchell, and D. J. Moss, "Highly Versatile Broadband RF Photonic Fractional Hilbert Transformer Based on a Kerr Soliton Crystal Microcomb," *Journal of Lightwave Technology,* vol. 39, no. 24, pp. 7581-7587, 2021.

[28] X. Xu, M. Tan, J. Wu, A. Boes, B. Corcoran, T. G. Nguyen, S. T. Chu, B. E. Little, R. Morandotti, A. Mitchell, and D. J. Moss, "Photonic RF and Microwave Integrator Based on a Transversal Filter With Soliton Crystal Microcombs," *IEEE Transactions on Circuits and Systems II: Express Briefs,* vol. 67, no. 12, pp. 3582-3586, 2020.

[29] X. Xu, M. Tan, B. Corcoran, J. Wu, T. G. Nguyen, A. Boes, S. T. Chu, B. E. Little, R. Morandotti, A. Mitchell, D. G. Hicks, and D. J. Moss, "Photonic Perceptron Based on a Kerr Microcomb for High‐Speed, Scalable, Optical Neural Networks," *Laser & Photonics Reviews,* vol. 14, no. 10, 2020.

[30] X. Xu, M. Tan, B. Corcoran, J. Wu, A. Boes, T. G. Nguyen, S. T. Chu, B. E. Little, D. G. Hicks, R. Morandotti, A. Mitchell, and D. J. Moss, "11 TOPS photonic convolutional accelerator for optical neural networks," *Nature,* vol. 589, no. 7840, pp. 44-51, Jan, 2021.

[31] J. Capmany, B. Ortega, D. Pastor, and S. Sales, "Discrete-time optical Processing of microwave signals," *Journal of Lightwave Technology,* vol. 23, no. 2, pp. 702-723, 2005.

[32] S. Mansoori, and A. Mitchell, "RF Transversal Filter Using an AOTF," *IEEE Photonics Technology Letters,* vol. 16, no. 3, pp. 879-881, 2004.

[33] J. Zhang, and J. Yao, "Photonic True-Time Delay Beamforming Using a Switch-Controlled Wavelength-Dependent Recirculating Loop," *Journal of Lightwave Technology,* vol. 34, no. 16, pp. 3923-3929, 2016/08/15, 2016.

[34] L. Zhang, M. Li, N. Shi, X. Zhu, S. Sun, J. Tang, W. Li, and N. Zhu, "Photonic true time delay beamforming technique with ultra-fast beam scanning," *Optics Express,* vol. 25, no. 13, pp. 14524-14532, 2017/06/26, 2017.

[35] G. Yu, W. Zhang, and J. A. R. Williams, "High-performance microwave transversal filter using fiber Bragg grating arrays," *IEEE Photonics Technology Letters,* vol. 12, no. 9, pp. 1183-1185, 2000.

[36] D. B. Hunter, R. A. Minasian, and P. A. Krug, "Tunable optical transversal filter based on chirped gratings," *Electronics Letters,* vol. 31, no. 25, pp. 2205-2207, 1995/12/07, 1995.

[37] Y. Liu, J. Yao, and J. Yang, "Wideband true-time-delay unit for phased array beamforming using discrete-chirped fiber grating prism," *Optics Communications,* vol. 207, no. 1-6, pp. 177-187, 2002.

[38] S. A. Diddams, D. J. Jones, J. Ye, S. T. Cundiff, J. L. Hall, J. K. Ranka, R. S. Windeler, R. Holzwarth, T. Udem, and T. W. Hansch, "Direct link between microwave and optical frequencies with a 300 THz femtosecond laser comb," *Phys Rev Lett,* vol. 84, no. 22, pp. 5102-5, May 29, 2000.

[39] D. J. Jones, S. A. Diddams, J. K. Ranka, A. Stentz, R. S. Windeler, J. L. Hall, and S. T. Cundiff, "Carrier-envelope phase control of femtosecond mode-locked lasers and direct optical frequency synthesis," *Science,* vol. 288, no. 5466, pp. 635-40, Apr 28, 2000.

[40] T. Udem, R. Holzwarth, and T. W. Hansch, "Optical frequency metrology," *Nature,* vol. 416, no. 6877, pp. 233-7, Mar 14, 2002.

[41] Y. Sun, J. Wu, M. Tan, X. Xu, Y. Li, R. Morandotti, A. Mitchell, and D. J. Moss, "Applications of optical microcombs," *Advances in Optics and Photonics,* vol. 15, no. 1, 2023.

[42] Y. Li, Y. Sun, J. Wu, C. E. Murray, G. Ren, X. Xu, B. Corcoran, S. T. Chu, B. E. Little, R. Morandotti, A. Mitchell, and D. J. Moss, "Feedback Control in Microwave Photonic Transversal Filter Systems Based on Optical Microcombs," *IEEE Journal of Selected Topics in Quantum Electronics,* vol. 30, no. 5: Microresonator Frequency Comb, pp. 1-17, 2024.

[43] L. Razzari, D. Duchesne, M. Ferrera, R. Morandotti, S. Chu, B. E. Little, and D. J. Moss, "CMOS-compatible integrated optical hyper-parametric oscillator," *Nature Photonics,* vol. 4, no. 1, pp. 41-45, 2009.

[44] M. Ferrera, L. Razzari, D. Duchesne, R. Morandotti, Z. Yang, M. Liscidini, J. E. Sipe, S. Chu, B. E. Little, and D. J. Moss, "Low-power continuous-wave nonlinear optics in doped silica glass integrated waveguide structures," *Nature Photonics,* vol. 2, no. 12, pp. 737-740, 2008.

[45] A. Pasquazi, M. Peccianti, L. Razzari, D. J. Moss, S. Coen, M. Erkintalo, Y. K. Chembo, T. Hansson, S. Wabnitz, P. Del'Haye, X. Xue, A. M. Weiner, and R. Morandotti, "Micro-combs: A novel generation of optical sources," *Physics Reports,* vol. 729, pp. 1-81, 2018.

[46] W. Wang, Z. Lu, W. Zhang, S. T. Chu, B. E. Little, L. Wang, X. Xie, M. Liu, Q. Yang, L. Wang, J. Zhao, G. Wang, Q. Sun, Y. Liu, Y. Wang, and W. Zhao, "Robust soliton crystals in a thermally controlled microresonator," *Optics Letters,* vol. 43, no. 9, pp. 2002-2005, 2018/05/01, 2018.

[47] D. C. Cole, E. S. Lamb, P. Del'Haye, S. A. Diddams, and S. B. Papp, "Soliton crystals in Kerr resonators," *Nature Photonics,* vol. 11, no. 10, pp. 671-676, 2017.

[48] M. Karpov, M. H. P. Pfeiffer, H. Guo, W. Weng, J. Liu, and T. J. Kippenberg, "Dynamics of soliton crystals in optical microresonators," *Nature Physics,* vol. 15, no. 10, pp. 1071-1077, 2019.

[49] C. Porzi, M. Reza, P. Ghelfi, M. Sorel, and A. Bogoni, "Silicon-on-Insulator Microwave Photonic Filter With Widely Tunable and Reconfigurable Flat-Top Bandpass Functionality," *Journal of Lightwave Technology,* vol. 40, no. 20, pp. 6666-6675, 2022.

[50] Y. Liu, Z. Pan, K. Cao, Y. Yu, F. Zhang, Y. Yu, and X. Zhang, "Reconfigurable Bandpass Microwave Photonic Filter Based on Cascaded Second-Order CROWs," *Journal of Lightwave Technology,* vol. 42, no. 16, pp. 5599-5605, 2024/08/15, 2024.

[51] Y. Sun, J. Wu, Y. Li, X. Xu, G. Ren, M. Tan, S. T. Chu, B. E. Little, R. Morandotti, A. Mitchell, and D. J. Moss, "Optimizing the Accuracy of Microcomb-Based Microwave Photonic Transversal Signal Processors," *Journal of Lightwave Technology,* vol. 41, no. 23, pp. 7223-7237, 2023.

[52] Y. Sun, J. Wu, Y. Li, M. Tan, X. Xu, S. T. Chu, B. E. Little, R. Morandotti, A. Mitchell, and D. J. Moss, "Quantifying the Accuracy of Microcomb-Based Photonic RF Transversal Signal Processors," *IEEE Journal of Selected Topics in Quantum Electronics,* vol. 29, no. 6: Photonic Signal Processing, pp. 1-17, 2023.

[53] H. Zhang, S. Zhang, T. Bi, G. Ghalanos, Y. Zhang, H. Yan, A. Pal, J. He, S. Pan, and P. Del'Haye, "Microresonator soliton frequency combs via cascaded Brillouin scattering," *Communications Physics,* vol. 8, no. 1, 2025.

[54] B. Bai, Q. Yang, H. Shu, L. Chang, F. Yang, B. Shen, Z. Tao, J. Wang, S. Xu, W. Xie, W. Zou, W. Hu, J. E. Bowers, and X. Wang, "Microcomb-based integrated photonic processing unit," *Nat Commun,* vol. 14, no. 1, pp. 66, Jan 5, 2023.

[55] H. Shu, L. Chang, Y. Tao, B. Shen, W. Xie, M. Jin, A. Netherton, Z. Tao, X. Zhang, R. Chen, B. Bai, J. Qin, S. Yu, X. Wang, and J. E. Bowers, "Microcomb-driven silicon photonic systems," *Nature,* vol. 605, no. 7910, pp. 457-463, May, 2022.

[56] L. Chang, S. Liu, and J. E. Bowers, "Integrated optical frequency comb technologies," *Nature Photonics,* vol. 16, no. 2, pp. 95-108, 2022.

[57] M. J. Strain, and M. Sorel, "Design and Fabrication of Integrated Chirped Bragg Gratings for On-Chip Dispersion Control," *IEEE Journal of Quantum Electronics,* vol. 46, no. 5, pp. 774-782, 2010.

[58] C. Wang, M. Zhang, X. Chen, M. Bertrand, A. Shams-Ansari, S. Chandrasekhar, P. Winzer, and M. Loncar, "Integrated lithium niobate

electro-optic modulators operating at CMOS-compatible voltages," *Nature,* vol. 562, no. 7725, pp. 101-104, Oct, 2018.

[59] M. H. Khan, H. Shen, Y. Xuan, L. Zhao, S. Xiao, D. E. Leaird, A. M. Weiner, and M. Qi, "Ultrabroad-bandwidth arbitrary radiofrequency waveform generation with a silicon photonic chip-based spectral shaper," *Nature Photonics,* vol. 4, no. 2, pp. 117-122, 2010.

[60] J. Michel, J. Liu, and L. C. Kimerling, "High-performance Ge-on-Si photodetectors," *Nature Photonics,* vol. 4, no. 8, pp. 527-534, 2010.

[61] Y. Sun, J. Wu, Y. Li, and D. J. Moss, "Comparison of Microcomb-Based Radio-Frequency Photonic Transversal Signal Processors Implemented with Discrete Components Versus Integrated Chips," *Micromachines (Basel),* vol. 14, no. 9, Sep 20, 2023.

62. Moss, D. J., Morandotti, R., Gaeta, A. L. & Lipson, M. New CMOS compatible platforms based on silicon nitride and Hydex for nonlinear optics. Nat. Photonics Vol. 7, 597-607 (2013).
63. L. Razzari, et al., "CMOS-compatible integrated optical hyper-parametric oscillator," Nature Photonics, vol. 4, no. 1, pp. 41-45, 2010.
64. A. Pasquazi, et al., "Sub-picosecond phase-sensitive optical pulse characterization on a chip", Nature Photonics, vol. 5, no. 10, pp. 618-623 (2011).
65. M Ferrera et al., "On-Chip ultra-fast 1st and 2nd order CMOS compatible all-optical integration", Optics Express vol. 19 (23), 23153-23161 (2011).
66. Bao, C., et al., Direct soliton generation in microresonators, Opt. Lett, 42, 2519 (2017).
67. M.Ferrera et al., "CMOS compatible integrated all-optical RF spectrum analyzer", Optics Express, vol. 22, no. 18, 21488 - 21498 (2014).
68. M. Kues, et al., "Passively modelocked laser with an ultra-narrow spectral width", Nature Photonics, vol. 11, no. 3, 159 (2017).
69. M. Ferrera, et al., "Low-power continuous-wave nonlinear optics in doped silica glass integrated waveguide structures," Nature Photonics, vol. 2, no. 12, pp. 737-740, 2008.
70. M.Ferrera et al."On-Chip ultra-fast 1st and 2nd order CMOS compatible all-optical integration", Opt. Express, vol. 19, (23)pp. 23153-23161 (2011).
71. D. Duchesne, M. Peccianti, M. R. E. Lamont, et al., "Supercontinuum generation in a high index doped silica glass spiral waveguide," Optics Express, vol. 18, no, 2, pp. 923-930, 2010.
72. H Bao et al., "Turing patterns in a fiber laser with a nested microresonator: Robust and controllable microcomb generation", Physical Review Research vol. 2 (2), 023395 (2020).
73. M. Ferrera, et al., "On-chip CMOS-compatible all-optical integrator", Nature Communications, vol. 1, Article 29 (2010).
74. A. Pasquazi, et al., "All-optical wavelength conversion in an integrated ring resonator," Optics Express, vol. 18, no. 4, 3858-3863 (2010).
75. A.Pasquazi, Y. Park, J. Azana, et al., "Efficient wavelength conversion and net parametric gain via Four Wave Mixing in a high index doped silica waveguide," Optics Express, vol. 18, no. 8, pp. 7634-7641 (2010).
76. Peccianti, M. Ferrera, L. Razzari, et al., "Subpicosecond optical pulse compression via an integrated nonlinear chirper," Optics Express, vol. 18, no. 8, pp. 7625-7633 (2010).
77. M. Ferrera et al., "All-optical 1st and 2nd order integration on a chip", Optics Express vol. 19 (23), 23153-23161 (2011).
78. M. Ferrera et al., "Low Power CW Parametric Mixing in a Low Dispersion High Index Doped Silica Glass Micro-Ring Resonator with Q-factor > 1 Million", Optics Express, vol.17, no. 16, 14098–14103 (2009).
79. M. Peccianti, et al., "Demonstration of an ultrafast nonlinear microcavity modelocked laser", Nature Communications, vol. 3, 765, 2012.
80. A. Pasquazi, et al., "Self-locked optical parametric oscillation in a CMOS compatible microring resonator: a route to robust optical frequency comb generation on a chip," Optics Express, vol. 21, no. 11, 13333-13341 (2013).
81. A. Pasquazi, et al., "Stable, dual mode, high repetition rate mode-locked laser based on a microring resonator," Optics Express, vol. 20, no. 24, 27355-27362 (2012).
82. Pasquazi, A. et al. "Micro-combs: a novel generation of optical sources", Physics Reports **729**, 1-81 (2018).
83. H. Bao, et al., "Laser cavity-soliton microcombs", Nature Photonics, vol. 13, no. 6, 384-389, (2019).
84. A. Cutrona et al., "High Conversion Efficiency in Laser Cavity-Soliton Microcombs", Optics Express Vol. 30, Issue 22, 39816-39825 (2022).
85. M. Rowley et al., "Self-emergence of robust solitons in a micro-cavity", Nature vol. **608** (7922) 303–309 (2022).
86. A. Cutrona et al., "Nonlocal bonding of a soliton and a blue-detuned state in a microcomb laser", ***Nature Communications Physics*** **6** Article 259 (2023).
87. Aadhi A. et al., "Mode-locked laser with multiple timescales in a microresonator-based nested cavity", ***APL Photonics*** **9** 031302 (2024).
88. A. Cooper et al., "Parametric interaction of laser cavity-solitons with an external CW pump", ***Optics Express*** **32** (12), 21783-21794 (2024).
89. A. Cutrona et al.,"Stability Properties of Laser Cavity-Solitons for Metrological Applications", Applied Physics Letters vol. 122 (12) 121104 (2023).
90. C. E. Murray et al., "Investigating the thermal robustness of soliton crystal microcombs", ***Optics Express*** **31**(23), 37749-37762 (2023).
91. Y. Sun et al., "Enhancing laser temperature stability by passive self-injection locking to a micro-ring resonator", ***Optics Express*** **32** (13) 23841-23855 (2024).
92. Y. Sun et al., "Applications of optical micro-combs", Advances in Optics and Photonics **15** (1) 86-175 (2023).
93. X. Xu et al.,"Reconfigurable broadband microwave photonic intensity differentiator based on an integrated optical frequency comb source," APL Photonics, vol. 2, no. 9, 096104 (2017).
94. Xu, X., et al., Photonic microwave true time delays for phased array antennas using a 49 GHz FSR integrated micro-comb source, Photonics Research, vol. 6, B30-B36 (2018).
95. X. Xu et al., "Microcomb-based photonic RF signal processing", IEEE Photonics Technology Letters, vol. 31 no. 23 1854-1857 (2019).
96. A. Aadhi, L. Di Lauro, B. Fischer, P. Dmitriev, I. Alamgir, C. Mazoukh, N. Perron, E. Viktorov, A. Kovalev, A. Eshaghi, S. Vakili, M. Chemnitz, P. Roztocki, B.E. Little, S. T. Chu, D. J. Moss, and R. Morandotti, "Scalable Photonic Reservoir Computing for Parallel Machine Learning Tasks", ***Nature Communications*** **17** (2026).
97. Yang Li, Yang Sun, Jiayang Wu, Guanghui Ren, Thach G. Nguyen, Bill Corcoran, Xingyuan Xu, Sai T. Chu, Brent E. Little, Roberto Morandotti, Arnan Mitchell, and David J. Moss, "Reconfigurable Microwave Photonic Filters with Ultrasteep Roll-Off Based on Optical Microcombs", ***Laser and Photonics Reviews*** **20** (2026). DOI: 10.1002/lpor.202501910.
98. Xu, et al., "Advanced adaptive photonic RF filters with 80 taps based on an integrated optical micro-comb source," Journal of Lightwave Technology, vol. 37, no. 4, 1288-1295 (2019).
99. X. Xu, et al., "Photonic RF and microwave integrator with soliton crystal microcombs", IEEE Transactions on Circuits and Systems II: Express Briefs, vol. 67, no. 12, 3582-3586 (2020).
100. X. Xu, et al., "High performance RF filters via bandwidth scaling with Kerr micro-combs," APL Photonics, vol. 4 (2) 026102 (2019).
101. M. Tan, et al., "Microwave and RF photonic fractional Hilbert transformer based on a 50 GHz Kerr micro-comb", Journal of Lightwave Technology, vol. 37, no. 24, 6097 – 6104 (2019).
102. M. Tan, et al., "RF and microwave fractional differentiator based on photonics", IEEE Transactions on Circuits and Systems: Express Briefs, vol. 67, no.11, 2767-2771 (2020).
103. M. Tan, et al., "Photonic RF arbitrary waveform generator based on a soliton crystal micro-comb source", Journal of Lightwave Technology, vol. 38, no. 22, 6221-6226 (2020).
104. M. Tan et al., "RF and microwave high bandwidth signal processing based on Kerr Micro-combs", Advances in Physics X, VOL. 6, NO. 1, 1838946 (2021).
105. X. Xu, et al., "Advanced RF and microwave functions based on an integrated optical frequency comb source," Opt. Express, vol. 26 (3) 2569 (2018).

106. M. Tan et al., "Highly Versatile Broadband RF Photonic Fractional Hilbert Transformer Based on a Kerr Soliton Crystal Microcomb", Journal of Lightwave Technology vol. 39 (24) 7581-7587 (2021).
107. Wu, J. et al., "RF Photonics: An Optical Microcombs' Perspective", IEEE Journal of Selected Topics in Quantum Electronics Vol. 24, 6101020, 1-20 (2018).
108. T. G. Nguyen et al., "Integrated frequency comb source-based Hilbert transformer for wideband microwave photonic phase analysis," Opt. Express, vol. 23, no. 17, 22087-22097, (2015).
109. X. Xu, et al., "Broadband RF channelizer based on an integrated optical frequency Kerr comb source," Journal of Lightwave Technology, vol. 36, no. 19, pp. 4519-4526, (2018).
110. X. Xu, et al., "Continuously tunable orthogonally polarized RF optical single sideband generator based on micro-ring resonators," Journal of Optics, vol. 20, no. 11, 115701 (2018).
111. X. Xu, et al., "Orthogonally polarized RF optical single sideband generation and dual-channel equalization based on an integrated microring resonator," Journal of Lightwave Technology, vol. 36, no. 20, 4808-4818 (2018).
112. X. Xu, et al., "Photonic RF phase-encoded signal generation with a microcomb source", J. Lightwave Technology, vol. 38, no. 7, 1722-1727 (2020).
113. X. Xu, et al., "Broadband microwave frequency conversion based on an integrated optical micro-comb source", Journal of Lightwave Technology, vol. 38 no. 2, 332-338 (2020).
114. M. Tan, et al., "Photonic RF and microwave filters based on 49GHz and 200GHz Kerr microcombs", Optics Communications vol. 465,125563 (2020).
115. X. Xu, et al., "Broadband photonic RF channelizer with 90 channels based on a soliton crystal microcomb", Journal of Lightwave Technology, Vol. 38, no. 18, 5116 – 5121 (2020).
116. M. Tan et al, "Orthogonally polarized Photonic Radio Frequency single sideband generation with integrated micro-ring resonators", IOP Journal of Semiconductors, Vol. 42 (4), 041305 (2021).
117. M. Tan et al., "Photonic Radio Frequency Channelizers based on Kerr Optical Micro-combs", IOP Journal of Semiconductors Vol. 42 (4), 041302 (2021).
118. B. Corcoran, et al., "Ultra-dense optical data transmission over standard fiber with a single chip source", Nature Communications, vol. 11, Article:2568, (2020).
119. X. Xu et al, "Photonic perceptron based on a Kerr microcomb for scalable high speed optical neural networks", Laser and Photonics Reviews, vol. 14, no. 8, 2000070 (2020).
120. X. Xu, et al., "11 TOPs photonic convolutional accelerator for optical neural networks", Nature vol. 589, 44-51 (2021).
121. X. Xu et al., "Neuromorphic computing based on wavelength-division multiplexing", ***IEEE Journal of Selected Topics in Quantum Electronics*** **29** (2) 7400112 (2023).
122. Y. Bai et al., "Photonic multiplexing techniques for neuromorphic computing", Nanophotonics vol. 12 (5): 795–817 (2023).
123. C. Prayoonyong et al., "Frequency comb distillation for optical superchannel transmission", Journal of Lightwave Technology vol. 39 (23) 7383-7392 (2021).
124. M. Tan et al., "Integral order photonic RF signal processors based on a soliton crystal micro-comb source", IOP Journal of Optics vol. 23 (11) 125701 (2021).
125. W. Han et al., "Dual-polarization RF Channelizer Based on Microcombs", ***Optics Express*** **32**, No. 7, 11281-11295 (2024).
126. W. Han et al., Photonic RF Channelization Based on Microcombs", ***IEEE Journal of Selected Topics in Quantum Electronics*** **30** (5) 7600417 (2024).
127. X. Xu et al., "Microcomb-enabled parallel self- calibration optical convolution streaming processor", ***Light Science and Applications*** (2025).
128. Z. Liu et al., "Advances in Soliton Crystals Microcombs", Photonics Vol. 11, 1164 (2024).
129. B.Corcoran et al., "Optical microcombs for ultrahigh-bandwidth communications", ***Nature Photonics*** Volume **19** (5) 451 - 462 (2025).
130. S. Chen et al "Integrated photonic neural networks", ***npj Nanophotonics*** **2**, 28 (2025).
131. Y. Li et al., "Feedback control in micro-comb-based microwave photonic transversal filter systems", ***IEEE Journal of Selected Topics in Quantum Electronics*** Vol. **30** (5) 2900117 (2024).
132. Y. Sun et al., "Optimizing the performance of microcomb based microwave photonic transversal signal processors", Journal of Lightwave Technology vol. 41 (23) 7223-7237 (2023).
133. M. Tan et al., "Photonic signal processor for real-time video image processing based on a Kerr microcomb", ***Nature Communications Engineering*** **2** 94 (2023).
134. Y. Sun et al., "Quantifying the Accuracy of Microcomb-based Photonic RF Transversal Signal Processors", IEEE Journal of Selected Topics in Quantum Electronics vol. 29 no. 6, 1-17, 7500317 (2023).
135. C. Mazoukh et al., "Genetic algorithm-enhanced microcomb state generation", ***Nature Communications Physics*** Vol. 7, 81 (2024).
136. S. Chen et al., "High-bit-efficiency TOPS optical tensor convolutional accelerator using micro-combs", ***Laser & Photonics Reviews*** **19** 2401975 (2025).
137. Y. Li et al., "Performance analysis of microwave photonic spectral filters based on optical microcombs", ***Advanced Physics Research*** **4** (9) 2400084 (2025).
138. L. di Lauro et al., "Optimization Methods for Integrated and Programmable Photonics in Next-Generation Classical and Quantum Smart Communication and Signal Processing", ***Advances in Optics and Photonics*** Vol. **17** (2) 526 - 622 (2025).
139. Y. Li et al., "Processing accuracy of microcomb-based microwave photonic signal processors for different input signal waveforms", ***Photonics 10***, 10111283 (2023).
140. Y. Sun et al., "Comparison of microcomb-based RF photonic transversal signal processors implemented with discrete components versus integrated chips", ***Micromachines*** **14**, 1794 (2023).
141. A. Aadhi, L. Di Lauro, B. Fischer, P. Dmitriev, I. Alamgir, C. Mazoukh, N. Perron, E. Viktorov, A. Kovalev, A. Eshaghi, S. Vakili, M. Chemnitz, P. Roztocki, B.E. Little, S. T. Chu, D. J. Moss, and R. Morandotti, "Scalable Photonic Reservoir Computing for Parallel Machine Learning Tasks", ***Nature Communications*** (2025).
142. Chengzhuo Xia, Yifu Xu, Shifan Chen, Sirui Huang, Yunping Bai, Sai T. Chu, Brent E. Little, Roberto Morandotti, David J. Moss, Xingyuan Xu, Kun Xu, " TOPS-speed Reconfigurable Photonic Transposed Convolution Accelerator for Generative Tasks", ***Laser & Photonics Reviews*** 0:e00771 (2025). https://doi.org/10.1002/lpor.202500771
143. M. Tan et al., "The laser trick that could put an ultraprecise optical clock on a chip", ***Nature*** **624**, (7991) 256-257 (2023).
144. J. Hu et al., "Thermo-optic response and optical bistablility of integrated high index doped silica ring resonators", ***Sensors*** **23** 9767 (2023).
145. Y. Zhang et al., "2D material integrated photonics: towards industrial manufacturing and commercialization", ***Applied Physics Letters Photonics*** **10**, 040903 (2025).
146. W. Jiang et al., "Enhanced thermo-optic performance for silicon microring resonators integrated with 2D graphene oxide films", ***ACS Applied Electronic Materials*** **7** (12), 5650-5661 (2025).
147. X. Yang et al., "Turnkey deterministic soliton crystal generation", ***Laser and Photonics Reviews*** **19** (10) 2401687 (2025).
148. Y. Sun et al., "Self-locking of free-running DFB lasers to a single microring resonator for dense WDM", ***Journal of Lightwave Technology*** **43**, (4) 1995-2002 (2025).
149. W. Han et al., "TOPS-speed complex-valued convolutional accelerator for feature extraction and inference", ***Nature Communications*** **16** 292 (2025).
150. J. Hu et al., "Silicon photonic polarizers incorporating 2D MoS2 films", Invited Paper, IEEE ***Journal of Selected Topics in Quantum Electronics*** **31** (2025). DOI:10.1109/JSTQE.2025.3610438
151. C. Khallouf et al., "Raman scattering and supercontinuum generation in high-index doped silica chip waveguides", Nonlinear Optics and its Applications, edited by John M. Dudley, Anna C. Peacock, Birgit Stiller, Giovanna Tissoni, SPIE Vol. 13004, 130040I (2024).
152. M. Zerbib et al., "Observation of Brillouin scattering in a high-index doped silica chip waveguide", ***Results in Physics*** **52** 106830 (2023).

153. C. Khallouf et al., “Raman scattering and supercontinuum generation in high-index doped silica chip waveguides”, Nonlinear Optics and its Applications, edited by John M. Dudley, Anna C. Peacock, Birgit Stiller, Giovanna Tissoni, SPIE Vol. 13004, 130040I (2024).
154. C. Khallouf et al., “Supercontinuum generation in high-index doped silica photonic integrated circuits under diverse pumping settings”, ***Optics Express*** **33**, 8431-8444 (2025).
155. C. Khallouf, L. Sader, A. Bougaud, G. Fanjoux, B. Little, S. T. Chu, D. J. Moss, R. Morandotti, G. P. Agrawal, J. M. Dudley, B. Wetzel, And T.Sylvestre, “Dual-pumping supercontinuum generation and temporal reflection in a nonlinear photonic integrated circuit”, ***Optics Express*** (2025).
156. A. Della Torre et al., “Mid-Infrared Supercontinuum Generation in a Varying Dispersion Waveguide for Multi-Species Gas Spectroscopy”, ***IEEE Journal of Selected Topics in Quantum Electronics*** **29** (1) 5100509 (2023).
157. Y. Yang et al., “Enhanced four-wave mixing in graphene oxide coated waveguides”, Applied Physics Letters Photonics vol. 3 120803 (2018).
158. Wu, J. et al., “Graphene oxide waveguide and micro-ring resonator polarizers”, Laser and Photonics Reviews Vol. 13, 1900056 (2019).
159. Y. Zhang et al., “Enhanced Kerr nonlinearity and nonlinear figure of merit in silicon nanowires integrated with 2D graphene oxide films”, ACS Applied Materials and Interfaces vol. 12 (29) 33094−33103 (2020).
160. Y. Qu et al., “Enhanced nonlinear four-wave mixing in silicon nitride waveguides integrated with 2D layered graphene oxide films”, Advanced Optical Materials vol. 8 (21) 2001048 (2020).
161. Shahaz S. Hameed, Di Jin, Aihao Zhao, Jiayang Wu, Junkai Hu, Sebastien Cueff, Christian Grillet, Yuning Zhang, Irfan H. Abidi, Sumeet Walia, Christelle Monat, and David J. Moss, “Enhanced self-phase modulation in silicon nitride waveguides integrated with 2D MoS2 films”, ***Advanced Materials Technologies*** **11** (2026). **DOI:** 10.1002/admt.202502349.
162. Rong Wang, Di Jin, Junkai Hu, Wenbo Liu, Yuning Zhang, Irfan H. Abidi, Sumeet Walia, Baohua Jia, Duan Huang, Jiayang Wu, and David J. Moss, “AI-guided design and optimization of 2D material based optical polarizers”, ***Chip*** (2026).
163. Rong Wang, Yijun Wang, Di Jin, Junkai Hu, Wenbo Liu, Yuning Zhang, Baohua Jia, Duan Huang, Jiayang Wu, and David J. Moss, “AI-guided optimization of integrated waveguide polarizers with 2D reduced graphene oxide”, ***JOSA B*** (2026).
164. J. Wu et al., “Enhanced nonlinear four-wave mixing in microring resonators integrated with layered graphene oxide films”, Small vol. 16 (16) 1906563 (2020).
165. J. Wu et al., “Graphene oxide waveguide polarizers and polarization selective micro-ring resonators”, Paper 11282-29, SPIE Photonics West, San Francisco, CA, 4 - 7 February (2020).
166. Y. Zhang et al., “Design and optimization of four-wave mixing in microring resonators integrated with 2D graphene oxide films”, Journal of Lightwave Technology Vol. 39 (20) 6553-6562 (2021).
167. Y. Qu et al., “Analysis of four-wave mixing in silicon nitride waveguides integrated with 2D layered graphene oxide films”, Journal of Lightwave Technology Vol. 39 (9) 2902-2910 (2021).
168. J. Wu et al., “Graphene oxide: versatile films for flat optics to nonlinear photonic chips”, Advanced Materials Vol. 33 (3) 2006415, 1-29 (2021).
169. Y. Qu et al., “Graphene oxide for enhanced optical nonlinear performance in CMOS compatible integrated devices”, Paper No. 11688-30, PW21O-OE109-36, 2D Photonic Materials and Devices IV, SPIE Photonics West, San Francisco CA March 6-11 (2021). doi.org/10.1117/12.2583978
170. Y. Zhang et al., “Optimizing the Kerr nonlinear optical performance of silicon waveguides integrated with 2D graphene oxide films”, Journal of Lightwave Technology Vol. 39 (14) 4671-4683 (2021).
171. Y. Qu et al., “Photo thermal tuning in GO-coated integrated waveguides”, Micromachines Vol. 13 1194 (2022).
172. Zhang Y et al., “Graphene oxide-based waveguides for enhanced self-phase modulation”, Annals of Mathematics and Physics Vol. 5 (2) 103-106 (2022). DOI:10.17352/amp.000048
173. Y. Zhang et al., “Enhanced spectral broadening of femtosecond optical pulses in silicon nanowires integrated with 2D graphene oxide films”, Micromachines Vol. 13 756 (2022).
174. Y. Zhang et al., “Enhanced supercontinuum generated in SiN waveguides coated with GO films”, ***Advanced Materials Technologies*** **8** (1) 2201796 (2023).
175. Y. Zhang et al.,“Graphene oxide for nonlinear integrated photonics”, ***Laser and Photonics Reviews*** **17** 2200512 (2023).
176. J. Wu et al., “Graphene oxide for electronics, photonics, and optoelectronics”, ***Nature Reviews Chemistry*** **7** (3) 162–183 (2023).
177. Y. Zhang et al., “Enhanced self-phase modulation in silicon nitride waveguides integrated with 2D graphene oxide films”, IEEE Journal of Selected Topics in Quantum Electronics Vol. 29 (1) 5100413 (2023).
178. Y. Qu et al., “Integrated optical parametric amplifiers in silicon nitride waveguides incorporated with 2D graphene oxide films”, ***Light: Advanced Manufacturing*** **4** 39 (2023).
179. J. Wu et al., “Novel functionality with 2D graphene oxide films integrated on silicon photonic chips”, ***Advanced Materials*** Vol. 36 2403659 (2024).
180. D. Jin et al., “Silicon photonic waveguide and microring resonator polarizers incorporating 2D graphene oxide films”, Applied Physics Letters, Vol. 125, 053101 (2024).
181. Y. Zhang et al., “Advanced optical polarizers based on 2D materials”, ***npj Nanophotonics*** **1**, 28 (2024).
182. J. Hu et al.,“2D graphene oxide: a versatile thermo-optic material”, ***Advanced Functional Materials*** **34** 2406799 (2024).
183. Y. Zhang et al., “Graphene oxide for enhanced nonlinear optics in integrated photonic chips”, Paper 12888-16, Conference OE109, 2D Photonic Materials and Devices VII, Chair(s): Arka Majmdar; Carlos M. Torres Jr.; Hui Deng, SPIE Photonics West, San Francisco CA, January 27 – February 1 (2024). Proceedings Volume 12888, 2D Photonic Materials and Devices VII; 1288805 (2024). https://doi.org/10.1117/12.3005069
184. D. Jin et al., “Thickness and Wavelength Dependent Nonlinear Optical Absorption in 2D Layered MXene Films”, ***Small Science*** **4** 2400179 (2024).
185. J. Hu et al., “Integrated waveguide and microring polarizers incorporating 2D reduced graphene oxide”, ***Opto-Electronic Science*** **4** 240032 (2025).
186. L. Jia et al., “Third-order optical nonlinearities of 2D materials at telecommunications wavelengths”, ***Micromachines***, **14** 307 (2023).
187. Linnan Jia, Jiayang Wu, Yuning Zhang, Yang Qu, Baohua Jia, Zhigang Chen, and David J. Moss, “Fabrication Technologies for the On-Chip Integration of 2D Materials”, Small: Methods Vol. 6, 2101435 (2022).
188. L. Jia et al., “BiOBr nanoflakes with strong nonlinear optical properties towards hybrid integrated photonic devices”, Applied Physics Letters Photonics vol. 4 090802 vol. (2019).
189. L. Jia et al “Large Third-Order Optical Kerr Nonlinearity in Nanometer-Thick PdSe2 2D Dichalcogenide Films: Implications for Nonlinear Photonic Devices”, ACS Applied Nano Materials vol. 3 (7) 6876–6883 (2020).
190. Kues, M. et al. “Quantum optical microcombs”, Nature Photonics vol. 13, (3) 170-179 (2019).
191. C.Reimer et al., “Integrated frequency comb source of heralded single photons,” Optics Express, vol. 22, no. 6, 6535-6546, (2014).
192. C. Reimer, et al., “Cross-polarized photon-pair generation and bi-chromatically pumped optical parametric oscillation on a chip”, Nature Communications, vol. 6, 8236, (2015).
193. L. Caspani et al., “Multifrequency sources of quantum correlated photon pairs on-chip: a path toward integrated Quantum Frequency Combs,” Nanophotonics, vol. 5, no. 2, pp. 351-362, (2016).
194. N. Montaut et al.,“Progress in integrated and fiber optics for time-bin based quantum information processing”, ***Advanced Optical Technologies*** **14** 1560084 (2025).
195. C. Reimer et al., “Generation of multiphoton entangled quantum states by means of integrated frequency combs,” Science, vol. 351, no. 6278, pp. 1176-1180, 2016.

196. M. Kues, et al., “On-chip generation of high-dimensional entangled quantum states and their coherent control”, Nature, vol. 546, no. 7660, pp. 622-626, 2017.
197. P. Roztocki et al., “Practical system for the generation of pulsed quantum frequency combs,” Optics Express, vol. 25, no. 16, pp. 18940-18949, 2017.
198. Y. Zhang, et al., “Induced photon correlations through superposition of two four-wave mixing processes in integrated cavities”, Laser and Photonics Reviews, vol. 14, no. 7, pp. 2000128, 2020.
199. C. Reimer, et al., “High-dimensional one-way quantum processing implemented on d-level cluster states”, Nature Physics, vol. 15, no.2, pp. 148–153, 2019.
200. P.Roztocki et al., “Complex quantum state generation and coherent control based on integrated frequency combs”, Journal of Lightwave Technology vol. 37 (2) 338-347 (2019).
201. S. Sciara et al., “Generation and Processing of Complex Photon States with Quantum Frequency Combs”, IEEE Photonics Technology Letters vol. 31 (23) 1862-1865 (2019).
202. H. Yu et al., “Quantum key distribution implemented with d-level time-bin entangled photons”, ***Nature Communications*** **16** 171 (2025).
203. H. Yu et al., “Exploiting nonlocal correlations for dispersion-resilient quantum communications”, ***Physical Review Letters*** **134** 220801 (2025).
204. S. Sciara et al., “Scalable and effective multilevel entangled photon states: A promising tool to boost quantum technologies”, Nanophotonics vol. 10 (18), 4447–4465 (2021).
205. L. Caspani et al., “Multifrequency sources of quantum correlated photon pairs on-chip: a path toward integrated Quantum Frequency Combs,” Nanophotonics, vol. 5, no. 2, 351-362, 2016.
206. H. Arianfard et al., “Sagnac interference in integrated photonics”, ***Applied Physics Reviews*** **10** (1) 011309 (2023).
207. H. Arianfard et al., “Optical analogs of Rabi splitting in integrated waveguide-coupled resonators”, ***Advanced Physics Research*** **2** 2200123 (2023).
208. H. Arianfard et al., “Spectral shaping based on optical waveguides with advanced Sagnac loop reflectors”, Paper PW22O-OE201-20, SPIE-Opto, Integrated Optics: Devices, Materials, and Technologies XXVI, SPIE Photonics West, San Francisco CA January 22 - 27 (2022).
209. Di Jin et al., “Modelling of complex integrated photonic resonators using scattering matrix method”, Photonics, Vol. 11, 1107 (2024).
210. H. Arianfard et al., “Spectral Shaping Based on Integrated Coupled Sagnac Loop Reflectors Formed by a Self-Coupled Wire Waveguide”, IEEE Photonics Technology Letters vol. 33 (13) 680-683 (2021).
211. H. Arianfard et al., “Three Waveguide Coupled Sagnac Loop Reflectors for Advanced Spectral Engineering”, Journal of Lightwave Technology vol. 39 (11) 3478-3487 (2021).
212. H. Arianfard et al., “Advanced Multi-Functional Integrated Photonic Filters based on Coupled Sagnac Loop Reflectors”, Journal of Lightwave Technology vol. 39 Issue: 5,1400-1408 (2021).
213. H. Arianfard et al., “Advanced multi-functional integrated photonic filters based on coupled Sagnac loop reflectors”, Paper 11691-4, PW21O-OE203-44, Silicon Photonics XVI, SPIE Photonics West, San Francisco CA March 6-11 (2021).
214. J. Wu et al., “Advanced photonic filters via cascaded Sagnac loop reflector resonators in silicon-on-insulator integrated nanowires”, Applied Physics Letters Photonics vol. 3 046102 (2018).
215. J. Wu et al., “Micro-ring resonator quality factor enhancement via an integrated Fabry-Perot cavity”, Applied Physics Letters Photonics vol. 2 056103 (2017).
216. T Ido et al., “Strained InGaAs/InAlAs MQW electroabsorption modulators with large bandwidth and low driving voltage”, IEEE photonics technology letters vol. 6 (10), 1207-1209 (1994).
217. D.J.Moss, S.Mclaughlin, G.Randall, M.Lamont, M. Ardekani, P.Colbourne, S.Kiran and C.A.Hulse, ”Multichannel tunable dispersion compensation using all-pass multicavity etalons”, Optical Fiber Communications Conference, Anaheim (2002) paper TuT2 page 132. Postconference Technical Digest (IEEE Cat. No.02CH37339). Opt Soc. America. Part vol.1, 2002, pp. 132-3. Washington, DC, USA.